# Spatially contrasted response of Devonian anoxia to astronomical forcing

Justin Gérard[1], Alexandre Pohl[2], Loïc Sablon[1], Jarno J.C. Huygh[3], Anne-Christine Da Silva[3], and Michel Crucifix[1]

[1]Université catholique de Louvain (UCLouvain), Earth and Life Institute (ELI), 1348 Louvain-la-Neuve, Belgium
[2]Université Bourgogne Europe, CNRS, Biogéosciences UMR 6282, 21000 Dijon, France
[3]University of Liège, SediCClim Department of Geology, Sart Tilman, 4000 Liège, Belgium

**Correspondence:** Justin Gérard (justin.gerard@uclouvain.be)

**Abstract.** The Devonian period, spanning from 419 to 359 million years ago, was marked by a warmer-than-present climate and recurring ocean anoxic events, with evidence increasingly suggesting a link between these events and astronomical forcing. Here, we explore how astronomical forcing influences ocean oxygenation by modulating the continental weathering flux of phosphate within a Late Devonian climate framework. To investigate this, we performed transient simulations spanning 1.1 Myr, crossing a 2.4 Myr eccentricity node using the cGENIE Earth system model. These simulations were driven by spatially resolved fluxes of reactive phosphorus from continents, computed using the emulator developed by Sablon et al. (2025), trained on GEOCLIM and HadSM3 outputs. Our results provide new evidence supporting eccentricity maxima as a driver of Late Devonian anoxic events. Additionally, global analysis reveals that obliquity variations can leave an imprint on global ocean oxygen levels via their influence on biological productivity, suggesting a potential pathway for obliquity-driven anoxia under greenhouse conditions. Regional analysis revealed pronounced spatial heterogeneity in the biogeochemical response to astronomical forcing. Local ocean circulation emerged as a critical factor in shaping these patterns. The simulations indicate that astronomical forcing can, through its impact on continental weathering fluxes, exert a dominant influence on ocean oxygenation, with regional oxygen concentrations varying by up to 35% and driving changes in regional anoxic volume of up to 19%. Finally, these findings help explain why proxy records from different locations may show divergent expressions of astronomical signals, potentially leading to contrasting interpretations of their role in driving ocean anoxia.

## 1 Introduction

Throughout the Devonian Period, multiple oceanic anoxic events (OAEs) occurred (Becker et al., 2020), with estimated durations ranging from $10^4$ to $10^6$ years (Kabanov et al., 2023). The Late Devonian, approximately 379–360 million years ago (Ma), was particularly marked by pronounced environmental crises and ocean anoxia, such as the well-known Kellwasser and Hangenberg events (Kaiser et al., 2016; Carmichael et al., 2019). There is still no consensus on the mechanisms responsible for the initiation and the duration of these Devonian OAEs (Haddad et al., 2018; Reershemius and Planavsky, 2021; Smart et al., 2023). Existing hypotheses include extensive volcanic activity (Ma et al., 2016; Paschall et al., 2019; Racki, 2020; Kabanov et al., 2023), the proliferation and expansion of terrestrial plants (Algeo and Scheckler, 1998; De Vleeschouwer et al., 2017;

Smart et al., 2023), climate cooling (Joachimski and Buggisch, 2002; Song et al., 2017; Huang et al., 2018; Pier et al., 2021), shifts in sea level and oceanic circulation dynamics (Wilde and Berry, 1984; Dopieralska, 2009; Chen et al., 2013), and changes in the position of the continents (Brugger et al., 2019; Gérard et al., 2025). There is also growing evidence that astronomical forcing could modulate at least some of these events, primarily through a "top-down" mechanism (Carmichael et al., 2019) whereby cyclic changes in temperature and precipitation alter continental nutrient fluxes to the ocean (De Vleeschouwer et al., 2014; Martinez and Dera, 2015; De Vleeschouwer et al., 2017; Wichern et al., 2024; Huygh et al., 2025). Specifically, studies conducted in Poland by De Vleeschouwer et al. (2013) identified that the deposition of anoxic black shales associated with the *Annulata*, Dasberg, and Hangenberg events is separated by approximately 2.4 million years (Myr). This suggests a role of eccentricity in the timing of these events, as the variance spectrum of eccentricity often contains such a cycle (Laskar et al., 2004). However, substantial uncertainties persist regarding the phase relationship of the astronomical forcing to the onset and development of Devonian OAEs. For instance, some cyclostratigraphic interpretations have reported the occurrence of the upper Kellwasser anoxic event, after a 2.4 Myr eccentricity minima (De Vleeschouwer et al., 2017; Da Silva et al., 2020; Wichern et al., 2024), while other studies reported strong obliquity and eccentricity, resulting in marine eutrophication leading to the upper Kellwasser Ma et al. (2022) and Huygh et al., (2025, under revision). Hence, these contrasting findings underscore the growing importance of better quantifying the contribution of astronomical forcing to Devonian oceanic oxygen levels and the pathways by which astronomical forcing may have modulated ocean oxygenation at that time.

Our objective is to assess the impact of astronomical forcing on ocean anoxia, specifically through the modulation of continental nutrient fluxes, within a Late Devonian climate context. To this end, we performed transient simulations using the Earth system model of intermediate complexity cGENIE (Ridgwell et al., 2007), coupled offline with a continental weathering flux of nutrients. This flux is computed using an emulator trained on outputs from the general circulation model (GCM) HadSM3 (Valdes et al., 2017) and the geochemical model GEOCLIM (Maffre et al., 2025), as developed in Sablon et al. (2025). By incorporating a GCM, we account for the changes in precipitation and evaporation caused by astronomical forcing more accurately than with the standard version of cGENIE. In addition to improving the representation of hydrological responses, this approach further enhances the simulation of nutrient fluxes to the ocean, limited in the standard cGENIE model version due to its non-dimensional treatment of continental weathering (Colbourn et al., 2013). This modelling framework allows, on the one hand, for a mechanistic assessment of how variations in orbital parameters (namely eccentricity, precession, and obliquity) affect terrestrial weathering rates and nutrient fluxes to the ocean, thereby influencing the development and spatial extent of anoxic conditions. On the other hand, the influence of astronomical forcing on oxygen levels through changes in ocean circulation is captured by cGENIE. A detailed description of the model configuration and experimental design is presented in Section 2. In Section 3.1, we examine the global characteristics of the transient coupled simulations, followed by a regional analysis in Section 3.2.

## 2 Methods

### 2.1 Models description

cGENIE is an Earth system model of intermediate complexity (Claussen et al., 2002) designed to simulate long-term interactions between climate, biogeochemical cycles, and ocean–atmosphere processes (Ridgwell et al., 2007). The ocean circulation component (3D) uses a frictional-geostrophic model to simulate the transport of heat, salinity, and biogeochemical tracers through advection, convection, and parametrised mixing. The sea ice module (2D) uses a simplified thermodynamic–dynamic scheme to compute ice thickness and fractional coverage based on thermal balances and surface flux exchanges. The atmospheric module (2D) is an energy–moisture balance layer that transports heat and humidity through advection and diffusion, with precipitation triggered by a humidity threshold. These three components form the C-GOLDSTEIN framework, fully described in Edwards and Marsh (2005) and Marsh et al. (2011). The BIOGEM module simulates ocean biogeochemistry, including nutrient-limited biological productivity and tracer cycling, and handles air–sea gas exchange processes. The ATCHEM module tracks atmospheric chemical species and computes their partial pressures to represent changes in atmospheric composition (Ridgwell et al., 2007). For this study, we used an open-system configuration version of cGENIE with regard to carbon and phosphorus (P), which includes the SEDGEM and ROKGEM modules. SEDGEM provides a representation of sedimentary stratigraphy and the preservation of biogenic carbonates and organic carbon ($C_{org}$) deposited on the seafloor (Ridgwell and Hargreaves, 2007; Hülse and Ridgwell, 2025). ROKGEM is a spatially explicit weathering module that simulates temperature- and runoff-dependent weathering rates, allowing dynamic feedbacks between climate, weathering, and the carbon cycle over multimillion-year timescales (Colbourn et al., 2013).

In the standard configuration of cGENIE, continental weathering is simply a function of the global mean continental temperature. This is inadequate to capture the effects of the astronomical forcing, as the latter primarily affects climate through changes in the spatial and seasonal distribution of incoming solar radiation (insolation). To address this, we replaced this simplified scheme with a state-of-the-art continental weathering module, which accounts for the coupled contributions of chemical weathering and erosion. Specifically, we used the framework described in Sablon et al. (2025) to couple cGENIE with a climate–weathering emulator. This emulator computes weathering fluxes under varying boundary conditions (orbital parameters and $pCO_2$) based on statistical relationships derived from outputs of HadCM3L, HadSM3 (the latter being the slab-ocean version of HadCM3) (Valdes et al., 2017), and GEOCLIM (used with fixed present-day average lithological fractions), explicitly accounting for the coupled contributions of chemical weathering and physical erosion to continental weathering. Both HadCM3L and HadSM3 were used, as the 81 HadSM3 simulations used to train the emulator required heat convergence flux data obtained from HadCM3L. The weathering fluxes are instantaneously routed from continental source cells to the closest ocean coastal grid cell via a nearest-neighbour scheme, which remains suitable given the similar grid layouts, both adapted from Scotese and Wright (2018), and the limited knowledge of the Late Devonian hydrological network. A detailed overview of GEOCLIM's continental weathering module is presented in Maffre et al. (2025), while a complete description of the emulator's architecture, training process, and topography is documented in Sablon et al. (2025) and repeated here for clarity (see Fig. 2).

The coupling between the emulator and cGENIE is deliberately minimal and targeted, replacing the continental nutrient flux of dissolved phosphate ($PO_4$) provided by cGENIE with values computed by the emulator. This replacement is performed offline every 1000 years, a frequency that is appropriate for capturing the long-term variability caused by the astronomical forcing. All other components and processes within the model remain unchanged, as our cGENIE setup uses a simplified, single-nutrient ($PO_4$) control on biological productivity (Ridgwell et al., 2007). In this configuration, biological productivity is driven by both [$PO_4$] availability and local insolation. An increase in surface $PO_4$ availability stimulates biological productivity, thereby enhancing microbial oxygen consumption through remineralization in the water column. Moreover, limiting the coupling to a single flux ensures that other variables computed by ROKGEM remain unaffected, maintaining consistency and simplicity in the overall setup. As a result, cGENIE now responds to spatially-resolved, astronomically-driven variations in continental $PO_4$ flux, thereby allowing a more robust investigation of the influence of orbital forcing on ocean anoxia.

In our simulations, the ocean is discretised on a 36×36 horizontal equal-area grid with 16 levels along the vertical that are logarithmically spaced (from 60 to 560 meters). We use the continental configuration on which the emulator from Sablon et al. (2025) was trained, namely that of Scotese and Wright (2018), which represents the palaeogeography at 370 Ma (see Fig. 1). As this continental reconstruction was also used in (Gérard et al., 2025), the large-scale ocean circulation patterns and associated diagnostics described there remain valid here; in particular, the overturning circulation shows only limited sensitivity to temperature changes (see their Fig. 7c). Because the modelled climate system is older than the mid-Mesozoic advent of open-ocean planktic calcifiers (approximately 200 Ma), the representation of calcium carbonate ($CaCO_3$) production is adapted accordingly (Ridgwell, 2005). Specifically, $CaCO_3$ production is restricted to shallow-marine carbonate platforms, spatially constrained based on the reconstructions of Kiessling et al. (2003). The surface albedo and zonally averaged wind stress profiles are prescribed from the HadCM3L simulation of Sablon et al. (2025), conducted with the same $pCO_2$ (926 ppm) as in Valdes et al. (2020) and an orbital configuration characterized by an eccentricity of 0, a longitude of perihelion of 0°, and an obliquity of 23°. These fields are incorporated into cGENIE using the open-source "muffingen" suite v0.9.24 (Ridgwell, 2023), and are held constant throughout the transient simulation. The solar constant is set to 1325 $W.m^{-2}$ based on Gough (1981), less than today because this younger Sun was also weaker. The atmospheric oxygen concentration is set to 80% of its present-day value to reflect the lower levels characteristic of the Late Devonian (Krause et al., 2018; Mills et al., 2023). The estimated climate sensitivity of cGENIE is approximately 3°C per doubling of $pCO_2$, which is close to the mean value from the Coupled Model Intercomparison Project (CMIP) 5 and slightly lower than that from CMIP6 (Zelinka et al., 2020). Ocean and atmosphere parameter values follow the standard cGENIE setup of Cao et al. (2009) and are identical to those in Pohl et al. (2022) and in Gérard et al. (2025). In our setup, the empirical equation proposed by Dunne et al. (2007) represents $C_{org}$ burial in marine sediments, while the empirical parameterization of Wallmann (2010) accounts for redox-dependent regeneration of P from sediments. Following Dunne et al. (2007), $C_{org}$ burial scales with the flux of organic matter reaching the seafloor and is therefore a function of surface ocean productivity. Following Wallmann (2010), a significant portion of P initially bound in organic matter is degraded in surface sediments and released into the ocean as dissolved $PO_4$. Furthermore, $PO_4$ release from sediments is enhanced under low-oxygen conditions in line with observations (Ingall and Jahnke, 1994). A detailed description of these schemes and their implementation in cGENIE is provided in Hülse and Ridgwell (2025).

### 2.2 Experimental setup

The astronomical forcing for the Devonian is not known precisely, due to the chaotic nature of the Solar System and the subtle, yet cumulative, effects of tidal dissipation on axial precession (Laskar et al., 2011). A series of plausible solutions is now available (Zeebe and Lantink, 2024), but our experiment design was finalised before that publication appeared. Nevertheless, the astronomical solution employed here shares the same frequency content and amplitude-modulation structure as those found across the Zeebe–Lantink ensemble. We adopted the same hybrid approach as Sablon et al. (2025). It relies, for planetary motion, on the solution by Laskar et al. (2011) (La11a), from which we extracted the interval between 123.3 Ma and 122.2 Ma. This interval features a resonance between the 2.4 Myr eccentricity period (associated with the *g4–g3* terms) and the 1.2 Myr obliquity modulation (associated with the *s4–s3* terms), as in most of the Cenozoic. This resonance is characterised by an increase in obliquity variance when eccentricity reaches a 2.4 Myr node, at which point its variance is lowest and the 100 thousand years (kyr) component of the eccentricity signal disappears. The node occurs approximately midway through the selected interval.

We coupled this solution with the precession model of Sharaf and Boudnikova (1967), following the procedure outlined in Berger and Loutre (1991). This involves first performing a harmonic decomposition of the planetary solution (using R code based on Šidlichovský and Nesvorný, 1997), and then specifying a reference obliquity and general precession rate. These reference values are given by Farhat et al. (2022) for the period around 370 Ma. With this construction, the solution yields obliquity frequencies of $30.555$ and $37.335$ years, and climatic precession frequencies of $16.470$ and $19.386$ years, which are considered plausible for the Late Devonian. The R code used to generate these time series is available in Crucifix (2025). We verified that the time series of obliquity and longitude of perihelion are nearly identical to those obtained by integrating, forward in time, the precession model of Laskar and Robutel (1993) with an appropriate Earth–Moon distance and dynamical ellipticity. The latter approach is admittedly more straightforward, but was not integrated into our workflow at the time the experiment was prepared.

The length and choice of this specific astronomical solution reflect a compromise between representativeness and computational feasibility, given that a 1.1 Myr simulation with cGENIE requires two months of continuous computation on our systems. In particular, we cannot know whether the (*g4–g3*) versus (*s4–s3*) resonance was active during the Devonian, but previous cyclostratigraphic interpretations assumed a well-expressed 2.4 Myr eccentricity node and pronounced obliquity cycles when crossing the node (De Vleeschouwer et al., 2017). The chosen solution satisfies these assumptions. Moreover, it conveniently includes within a single sequence a transition from well-expressed 100 kyr eccentricity cycles modulated by a 405 kyr cycle, to the 2.4 Myr node (during which the 100 kyr cycles disappear), and then back to well-expressed 100 kyr eccentricity cycles. For reference, we use the heliocentric convention for expressing the longitude of perihelion, which is therefore $0^\circ$ when perihelion occurs in September (as in Sablon et al., 2025 and Gérard et al., 2025).

cGENIE reached equilibrium through a two-step spin-up process similar to Ridgwell and Hargreaves (2007), Hülse and Ridgwell (2025) and Vervoort et al. (2024). In the initial spin-up phase (SPIN1), ocean dynamics and biogeochemical cycling equilibrate with fixed atmospheric $pCO_2$ and $\delta^{13}C$ under a closed system. Burial of $CaCO_3$, $C_{org}$, and P are balanced by global

weathering inputs, and the resulting data are used to determine global equilibrium burial rates. The second spin-up phase (SPIN2) uses an open-system setup, with weathering fluxes set to the equilibrium with burial rates from SPIN1 and allowed to respond to temperature. A complete description of this two-step procedure in cGENIE, including $C_{org}$ and P feedbacks, is detailed in Hülse and Ridgwell (2025). We found that during the SPIN2, the model exhibited significant drift, most notably in $pCO_2$, with the system requiring up to 500 kyr to reach equilibrium. To address this, we heuristically adjusted the initial $pCO_2$ concentration in SPIN1 to guide the model toward a geochemically consistent Late Devonian state. Part of this consistency has already been achieved by estimating the initial mean $PO_4$ concentration based on outputs from GEOCLIM. By the end of SPIN2, the system reached an atmospheric $pCO_2$ concentration of approximately 550 ppm, consistent with the estimates of Chen et al. (2021) and Dahl et al. (2022), and an average surface $PO_4$ concentration of 0.47 $\mu$mol.kg$^{-1}$, in agreement with Sharoni and Halevy (2023). Furthermore, the system achieved modern-like burial fluxes (similar to Hülse and Ridgwell, 2025), including 0.144 PgC.yr$^{-1}$ of $CaCO_3$ (reef only) (Frankignoulle and Gattuso, 1993), 0.075 PgC.yr$^{-1}$ of $C_{org}$ (Dunne et al., 2007; Bradley et al., 2022), and 0.062 Tmol.yr$^{-1}$ of P (Benitez-Nelson, 2000; Ruttenberg, 2003). The cause of this drift remains unclear, but our testing indicates that drift is affected by the continental configuration and model resolution. A full investigation of its origin lies beyond the scope of this study, as it would require substantial computational time, with a 500 kyr simulation requiring roughly one month of runtime.

Starting from the equilibrium state (SPIN2), the continental $PO_4$ nutrient flux provided by cGENIE is replaced with values computed by the emulator. The model is then run for an additional 100 kyr with astronomical parameters fixed at their average value across the adopted astronomical solution, allowing the system to adjust to the new $PO_4$ flux boundary condition. This average astronomical configuration is characterised by an eccentricity of 0.027, an obliquity of 0.388 rad (22.23°) (Farhat et al., 2022) and longitude of perihelion set to 90° ($\sin \varpi = 1$). To ensure continuity, the global average flux of $PO_4$ computed by the emulator is rescaled (decreased by approximately 10%) to perfectly align with the global average flux of $PO_4$ computed by the built-in weathering module of cGENIE at the end of SPIN2. Following this adaptation period, a series of 3 transient simulations spanning the full 1.1 Myr astronomical solution were conducted. These include: (1) a run with all astronomical parameters evolving (Full); (2) a sensitivity experiment with only obliquity varying while eccentricity and precession were held constant at their average values (Obli); (3) a run in which only eccentricity and precession vary, with obliquity fixed at its average value (Ecc-prec). Simulations description is summarized in Table 1. Additionally, a control simulation was performed in which all astronomical parameters were held constant at their mean values.

## 3 Results

### 3.1 Moderate global astronomical influence

The global time series of atmospheric $pCO_2$, oceanic $PO_4$, and dissolved $O_2$ concentrations ($[PO_4]$ and $[O_2]$ respectively) for each transient simulation conducted across the astronomical solution are shown in Fig. 3. Throughout the reference simulation with all astronomical parameters evolving (black line in Fig. 3), atmospheric $pCO_2$ fluctuates by up to 40 ppm around a mean value of 555 ppm, driven by interactions within the open carbon cycle (ROKGEM and $C_{org}$ burial). In the ocean,

globally-averaged [$PO_4$] varies by approximately 0.1 $\mu$mol.kg$^{-1}$ around a mean of 2.67 $\mu$mol.kg$^{-1}$, while global mean [$O_2$] remains within a range of 5 $\mu$mol.kg$^{-1}$ around an average of 54 $\mu$mol.kg$^{-1}$ (see Appendix). The temporal variability of both atmospheric $pCO_2$ and oceanic [$PO_4$] is almost exclusively driven by the combined forcings of eccentricity and precession, with obliquity playing a very minor role (see Fig. 3a and b). Overall, variations in global mean concentrations caused by astronomical forcing remain of moderate amplitude. This is consistent with the results of Sablon et al. (2025) and unsurprising considering that global averages can mask spatially heterogeneous responses, including contrasting and potentially compensating regional signals.

Atmospheric $pCO_2$ and oceanic [$PO_4$] evolve in anti-phase throughout the simulation (see black and red curves in Fig. 3a and b). This inverse relationship occurs because intensified weathering simultaneously enhances $CO_2$ consumption and increases the continental flux of $PO_4$ to the ocean, leading to lower atmospheric $pCO_2$ and higher oceanic [$PO_4$]. The dominant control of eccentricity and precession on atmospheric $pCO_2$ and oceanic [$PO_4$] arises from their pronounced effect on continental weathering fluxes. Specifically, these two orbital parameters can drive changes in $PO_4$ delivery to the ocean of up to 9.5%, compared to only about 1.5% under obliquity-driven forcing alone. When all three orbital parameters evolve simultaneously, this modulation can reach 10.5%. In our simulations, the dominant driver is the precession-sensitive monsoon system captured by the emulator: precession alters monsoon intensity and distribution, which directly modulates the spatial pattern of runoff and thus weathering and $PO_4$ delivery. Beyond this, eccentricity is positively correlated with $PO_4$ weathering, such that periods of high eccentricity are associated with enhanced oceanic [$PO_4$], a feature already identified and documented in Sablon et al. (2025).

A global low-oxygen state characterises the ocean in these simulations (see Fig. 3c) compared to the modern climate (Schmidtko et al., 2017; Garcia et al., 2024), consistent with the findings of Gérard et al. (2025) under similar boundary conditions and the estimations made by Tostevin and Mills (2020) based on long-term geochemical proxy data. While all three orbital parameters affect global-mean [$O_2$], they operate through distinct mechanisms. Eccentricity and precession primarily influence global [$O_2$] by modulating the oceanic $PO_4$ inventory. The relationship between globally-averaged [$PO_4$] and [$O_2$] is evidenced by a strong correlation ($R^2$ = 0.82 and p-value = 0.016)[1] between the two red curves in Fig. 3b and c. These [$PO_4$] variations arise from changes in the continental weathering flux of $PO_4$, with high eccentricity associated with reduced global [$O_2$]. In contrast, obliquity exerts only a very weak effect on global [$PO_4$] that is insufficient to explain the simulated [$O_2$] variations. This is reflected by the almost absent correlation ($R^2$ = 0.06 and p-value = 0.467) between the two blue curves in Fig. 3b and c. Instead, obliquity primarily influences global [$O_2$] through its strong modulation of high-latitude insolation, as also noted by Gérard et al. (2025). Because modelled biological productivity explicitly depends on local insolation (Ridgwell et al., 2007), obliquity substantially alters oxygen consumption in these regions. These variations lead to changes in subsurface (around 60–130 m depth) [$O_2$] of up to 4 $\mu$mol.kg$^{-1}$. As these [$O_2$] anomalies emerge in deep-water formation zones, they are efficiently distributed throughout the global ocean via large-scale overturning circulation, resulting in consistent oxygen variations of approximately 4 $\mu$mol.kg$^{-1}$ across the benthic ocean (not shown). Consequently, times of high obliquity are asso-

[1] All presented statistics account for the temporal autocorrelation inherent in our setup, using an effective sample size correction based on the $N_{eff}$ method, following the approach of Bretherton et al. (1999).

ciated with decreased global [$O_2$], driven by increased biological productivity in high-latitude regions. There, the productivity anomalies driven by obliquity are more than three times larger than those caused by eccentricity and precession combined. Hence, the combination of high eccentricity and high obliquity results in the most severe depletion of simulated global [$O_2$] (see Fig. 3c and d).

### 3.2 High regional variability

To assess regional expressions of [$O_2$] variability driven by astronomical forcing, we defined distinct regions, as shown together with their associated watersheds in Fig. 4a and b. They are named after their approximate paleogeographic positions: region SA (South America), region WL (western Laurussia), region Si (Siberia), region NP (northern pole), and region LG (Laurussia–Gondwana). These regions were initially constrained by the depth distribution of Devonian anoxia proxy data, which predominantly originates from shallow-marine settings. Because the ocean floor from the Devonian period has been lost to subduction and plate tectonic processes, proxies for deep-water properties are scarce (Granot, 2016; Scotese and Wright, 2018). Consequently, grid cells deeper than 1000 meters were excluded, except for those associated with deep-water formation, which occurs in regions SA and NP. Within this depth-limited framework, we further refined the regions by grouping model grid points based on the temporal variance of [$PO_4$] and [$O_2$] (see Appendix A), with the final result shown in Fig. 4a. Hence, this approach enables us to assess whether astronomical forcing triggers distinct biogeochemical responses across various regions.

Fig. 4c displays the time series of regionally-averaged [$O_2$] and anoxic volume anomalies, for each region (as defined in Fig. 4a), in the reference simulation with all astronomical parameters evolving concurrently (Full). The results highlight a marked spatial heterogeneity in the biogeochemical response to astronomical forcing. On the one hand, regions SA and LG exhibit strong sensitivity to astronomical variability. In these regions, [$O_2$] fluctuates by 45 and 19.5 $\mu$mol.kg$^{-1}$, respectively, equivalent to a 35% deviation from their regional means. Simulated [$O_2$] reach their lowest values during periods of maximum eccentricity. These pronounced oxygen variations translate into substantial changes in anoxic volume, reaching approximately 19% in region SA and 13.5% in region LG. On the other hand, region Si is mostly unaffected by astronomical forcing. Temporal variability in both [$O_2$] and anoxic volume is limited to approximately 5% and 2.5%, respectively, with the anoxic volume remaining stable throughout most of the simulation. Although the signal is subtle in magnitude, region Si exhibits an opposite precession phasing compared to regions SA and LG, a feature resulting from their locations in different hemispheres. Region NP exhibits no anoxic conditions over the period, because of its consistently high [$O_2$] and the limited magnitude of [$O_2$] variations, which are insufficient for any grid cell in the region to cross the anoxic threshold. These high [$O_2$] values over region NP are expected given the presence of major deep water formation in this region, whereas the relatively weaker deep water formation in region SA explains why this region can exhibit anoxia (see Fig. A1e and Fig. A2).

The relative influence of individual astronomical parameters is clarified by the power spectrum analysis of the [$O_2$] time series (Fig. 5). Precession emerges as the dominant driver of [$O_2$] variability in regions SA, WL, Si, and LG, while [$O_2$] in region NP is primarily shaped by obliquity. Although eccentricity produces no distinct spectral peak, it remains essential

through its modulation of precession amplitude (see Fig. 4c). Notably, periods of high eccentricity tend to coincide with decreased oxygen levels across all regions, underscoring its consistent impact.

By definition, variations in anoxic volume arise from changes in regional $[O_2]$. Typically, these $[O_2]$ fluctuations are closely tied to changes in biological productivity and subsequent demineralization. In regions SA, WL, and LG, $[O_2]$ variability is almost entirely driven by variations in the $[PO_4]$ component of biological productivity (regional $R^2 \geq 0.75$ and p-values $< 10^{-3}$). In region NP, $[O_2]$ variability aligns closely with the insolation component of biological productivity ($R^2 = 0.66$ and p-value $< 10^{-3}$), whereas the $[PO_4]$ component shows no meaningful relationship ($R^2 = 0.01$, p-value = 0.63). This indicates that insolation-forced biological productivity, rather than $[PO_4]$, controls $[O_2]$ dynamics in this region. Region Si exhibits a distinct behaviour compared with all others. It is the only region where $[O_2]$ variability is not primarily driven by biological productivity ($R^2 = 0.22$ and p-value $< 10^{-3}$), indicating the dominance of another mechanism. The strong correspondence between $[O_2]$ in region Si and the northern hemisphere mean ($R^2 = 0.79$, p-value $< 10^{-3}$) suggests that large-scale physical transport and mixing, consistent with strong currents and circulation in this region (see Fig. 7), drive these regional $[O_2]$ fluctuations. Overall, our results indicate that when regional $[O_2]$ variability is high, it is primarily driven by the $[PO_4]$ component of biological productivity. However, when $[PO_4]$ fluctuations are limited, other processes, such as insolation-forced changes in biological productivity or large-scale advection and mixing, become more critical.

With the link between $[PO_4]$ and $[O_2]$ established, we now turn to the drivers of $[PO_4]$ variability. Figure 6 shows the time series of average $[PO_4]$ and $PO_4$ weathering, in addition to the linear regression between these two quantities for each region. Region NP has been excluded because there is no direct regional weathering flux of $PO_4$ coming from the continents. For correlation analysis, the $[PO_4]$ time series for each region (except region Si) was slightly shifted to best align with the weathering time series. This adjustment accounts for the natural time lag between the two quantities, as $[PO_4]$ typically increases when the weathering flux of $PO_4$ is high. Namely, even as continental weathering begins to decrease, $[PO_4]$ continues to rise as long as the $PO_4$ input to a given region temporarily exceeds the rate at which it is consumed, producing a lag of several thousand years between the weathering signal and the $[PO_4]$ response (see Fig. 6). To ensure the mechanism remains consistent with an astronomical-forcing interpretation, this lag was chosen to maximize the correlation but was limited to a maximum of 5 kyr (approximately one-fourth of a precession cycle). Because both the magnitude of the $PO_4$ weathering peak and the rate at which $PO_4$ is consumed through biological productivity differ across regions, the resulting lag is region-specific. When a negative lag is applied to $[PO_4]$ in regions SA, WL, and LG, it becomes clear that regional weathering accounts for most of the variations in $[PO_4]$. Hence, in these regions, variations in $[O_2]$ and anoxic extent are predominantly driven by regional $[PO_4]$, hence $PO_4$ weathering, which in turn is mainly modulated by eccentricity and precession (see Fig. 6).

In region Si, the relationship between $[PO_4]$ and $PO_4$ weathering differs fundamentally from that of all other regions. Unlike SA, WL, and LG, where regional $PO_4$ weathering clearly imprints on $[PO_4]$, no meaningful correspondence emerges in region Si. The regional $PO_4$ weathering flux is comparatively weak (about half that of region LG), and strong currents promote rapid advection and mixing, preventing local accumulation of weathered $PO_4$ (see Fig. 7). As a result, regional $[PO_4]$ variations do not reflect local weathering input. Instead, $[PO_4]$ in region Si closely follows the broader Northern Hemisphere signal ($R^2 =$

0.98 and p-value < $10^{-3}$), indicating that large-scale transport governs its temporal evolution. This behaviour is consistent with the mechanism identified earlier: circulation and mixing dominate both $[O_2]$ and $[PO_4]$ variability in region Si.

## 4 Discussion

### 4.1 Implications

We used cGENIE with an upgraded representation of weathering taken from Sablon et al. (2025), to investigate the influence of astronomical forcing on Late Devonian ocean oxygenation. Our simulations indicate that the Late Devonian background state was already characterised by low oceanic $[O_2]$, which likely contributed to the increased frequency of anoxic events observed throughout this period (Becker et al., 2020). We found that astronomical forcing leaves a discernible imprint on the global time series of atmospheric $pCO_2$, oceanic $[PO_4]$, and dissolved $[O_2]$. Notably, the evolution of atmospheric $pCO_2$ under astronomical forcing closely mirrors the results reported by Sablon et al. (2025), exhibiting a similar amplitude of approximately 40 ppm, with higher atmospheric $pCO_2$ concentrations corresponding to periods of minimum eccentricity. A similar $pCO_2$ range was also obtained by Vervoort et al. (2024) when running cGENIE with astronomical forcing, using a very different experimental setup featuring an idealized continental configuration and no representation of $C_{org}$ burial. In our simulations, $[O_2]$ variations primarily occur through the influence of eccentricity and precession on continental weathering fluxes, as well as obliquity on high-latitude biological productivity. Periods of combined high eccentricity and high obliquity produce the most pronounced deoxygenation, although global mean $[O_2]$ variations remain within a modest magnitude range of 5 $\mu$mol.kg$^{-1}$ throughout the simulations. Because the ocean exhibits substantial spatial heterogeneity in benthic $[O_2]$, with differences reaching 100 $\mu$mol.kg$^{-1}$, it is unlikely for the simulated $[O_2]$ variations to drive global-scale benthic areas below the anoxia threshold. Based on our modelling, it is thus highly implausible that the astronomical forcing alone could induce an anoxic event over the entire global ocean (i.e., including the benthic ocean).

Building on the global-scale analysis, we performed a more localized investigation by defining specific regions to capture potentially distinct biogeochemical dynamics induced by astronomical forcing. The results reveal that eccentricity maxima commonly coincide with the most pronounced anoxic extent, supporting the proposal by Ma et al. (2022) and Huygh et al. (2025) that the Upper Kellwasser coincide with an eccentricity maxima configuration. However, both the magnitude and the dominant astronomical parameter driving this response vary markedly across regions, underscoring the spatial heterogeneity captured in our simulations. While certain regions exhibit strong sensitivity to astronomical forcing, with $[O_2]$ varying by up to 35% and the anoxic volume by up to 19%, others remain largely unaffected. Regions near continental margins (i.e., more directly influenced by weathering fluxes) exhibit a strong precessional control, with the largest variations in $[O_2]$ and anoxic volume occurring in these weathering-dominated settings. This influence is not limited to low-latitude areas; for instance, region SA exhibits a notable precession signal despite its relatively high latitude, whereas precession is generally thought to primarily affect low latitudes due to its strong control on precipitation patterns (De Vleeschouwer et al., 2012). In contrast, high-latitude regions far from continental margins (i.e., less directly influenced by weathering fluxes) are more sensitive to obliquity-driven changes, particularly through their influence on the insolation component of biological productivity. These findings

underscore the pivotal role of $PO_4$ weathering and biological productivity in shaping regional biogeochemical responses, aligning with the 'top-down' hypothesis proposed in Carmichael et al. (2019). However, physical processes such as ocean circulation and tracer advection can override this control, as exemplified in region Si, where local $[O_2]$ and $[PO_4]$ dynamics are decoupled from regional weathering due to strong transport. Our results further demonstrate how regions SA, WL and LG, characterized by relatively weak surface circulation, provide ideal conditions for astronomically driven weathering variations to leave a substantial imprint on local $[O_2]$.

Altogether, these results demonstrate that astronomical forcing can exert pronounced control on ocean biogeochemistry, with its impact shaped by local physical conditions. Furthermore, the regional analysis of the shallow ocean suggests that an astronomical signal may appear globally distributed across the observational record. However, it also indicates that proxy records from distinct locations may reflect fundamentally different expressions of an astronomical signal, potentially leading to contrasting interpretations of its role in driving ocean anoxia.

Despite the important contribution that astronomical forcing can exert on $[O_2]$, the biogeochemical response of the system remains relatively simple when compared to the forcing. Specifically, the regions often exhibit a quasi-linear response to the forcing, lacking clear signs of long-term memory effects or strong non-linearities. This is particularly surprising given that redox-dependent P regeneration is represented in our model configuration (using the scheme from Wallmann, 2010), a feature explicitly proposed in Percival et al. (2020) to explain the sustainability of Late Devonian anoxia based on the investigation of sedimentary concentrations. Hence, the absence of prolonged anoxia in our simulations indicates that the $PO_4$ variations induced by astronomical forcing may be either too gradual or too limited in amplitude to trigger or maintain an anoxic state over extended timescales in our experimental setup (e.g., $10^5$ years). Our results also suggest that anoxic events could manifest as a series of smaller, short-lived, precession-paced episodes (see Fig. 4c and supplementary video) rather than a single, prolonged global event, similar to the scenario proposed by Hedhli et al. (2023). These findings motivate future studies centred on additional processes that may influence the system response, including vegetation–climate interactions driven by orbital forcing and the effects of large, episodic nutrient inputs. In particular, assessing the persistence and biogeochemical consequences of such perturbations could help constrain the conditions under which sustained anoxia might emerge.

### 4.2 Limitations

Because cGENIE is a relatively simple model, it suffers from well-known intrinsic limitations. Among these are its coarse spatial resolution, resulting in a simplified representation of continental geometry and shallow-water environments, the absence of explicitly resolved atmospheric dynamics, a basic hydrological scheme, and the lack of ice-sheet dynamics. Nevertheless, cGENIE has been widely used in previous studies and has demonstrated its capacity to reproduce large-scale ocean circulation features (Rahmstorf et al., 2005; Lunt et al., 2006; Cao et al., 2009; Marsh et al., 2013; Pohl et al., 2022; Gérard and Crucifix, 2024; Laridon et al., 2025) and to accurately simulate key aspects of ocean biogeochemistry (Ridgwell et al., 2007; Ridgwell and Hargreaves, 2007; Colbourn et al., 2013; Ward et al., 2018; Adloff et al., 2020; Reinhard et al., 2020; Crichton et al., 2021; Van De Velde et al., 2021; Naidoo-Bagwell et al., 2024; Stappard et al., 2025). These studies collectively demonstrate the model's reliability in simulating paleoclimate conditions and associated biogeochemical responses. Furthermore, some of

these limitations are addressed by our specific experimental design. The prescribed wind stress field, although not responsive to climate variability, was derived from HadCM3L simulations conducted by Sablon et al. (2025). To evaluate the implications of this assumption, we performed a sensitivity experiment using wind stress and albedo fields from an available HadCM3L simulation forced with an extreme orbital configuration (eccentricity of 0.08, obliquity of 25°, and precession of 45°), as required for the emulator training strategy of (Sablon et al., 2025). Even under this extreme configuration, the resulting $[O_2]$ variations (3 $\mu$mol.kg$^{-1}$ globally and 16, 3, 9, 8, and 10 $\mu$mol.kg$^{-1}$ for regions SA, WL, Si, NP, and LG) remain generally smaller than those driven by orbitally paced phosphate weathering in our main experiments (5 $\mu$mol.kg$^{-1}$ globally and up to 45, 9, 6, 7, and 19 $\mu$mol.kg$^{-1}$ regionally). More generally, the emulator accounts for changes in precipitation associated with variations in astronomical configuration and atmospheric $pCO_2$, thereby improving the representation of hydrological controls on $PO_4$ weathering. Together, these features enable a more realistic representation of two central climate components in our study: $PO_4$ weathering and ocean circulation.

Still, several important limitations of our approach carry implications for interpreting the results. Our results could depend on the selected paleogeographic reconstruction, given the substantial uncertainties that persist in deep-time topography and, by extension, in slope, erosion, and weathering patterns. It would therefore be valuable for future studies to assess how alternative reconstructions, such as those from Vérard (2019) or Cermeño et al. (2022), might influence these processes and the resulting oceanic response. Moreover, a simple nearest-neighbour scheme was used to route continental weathering products into the ocean; alternative watershed configurations could yield significantly different regional responses to astronomical forcing. Similarly, the use of HadCM3L, HadSM3, and GEOCLIM necessarily reflects one possible representation of climate and weathering dynamics; alternative emulator models or hydrological schemes could yield quantitatively different outcomes, although assessing the magnitude of such differences would require dedicated sensitivity experiments. The current setup also does not capture extreme events that may substantially influence sedimentary fluxes, and relies on a simplified organic matter sedimentation scheme that lacks oxygen dependence, highlighting the potential benefit of integrating more advanced models of organic matter diagenesis like OMEN-SED (Hülse et al., 2018) in future work. Additionally, the surface wind stress field is held constant throughout the simulations, preventing realistic changes in circulation patterns in response to evolving astronomical configurations. The exclusion of ice sheets and sea-level variations removes critical mechanisms through which obliquity can strongly impact $[O_2]$, although the accurate representation of sea-level changes would remain challenging at the cGENIE grid resolution. Several studies have suggested that these processes may have contributed to, or exacerbated, Late Devonian anoxic events (Bond and Wignall, 2008; Chen et al., 2013; Huygh et al., 2025). As a result, the influence of obliquity identified in this study may be underestimated, though it still leaves a discernible imprint on the global ocean. For all these reasons, we emphasize the importance of further modelling efforts to better connect orbital forcing with ocean anoxia. For instance, subsequent work would benefit from incorporating dynamic albedo and wind-stress profiles when exploring the full range of climate-circulation–biogeochemistry interactions. This is further encouraged by the results of Sarr et al. (2022), who showed that astronomically driven changes in ocean circulation and ventilation can exert a strong control on oxygenation, with regional variations reaching up to 40 $\mu$mol.kg$^{-1}$ in a Late Cretaceous context. They could also explicitly test the robustness of the Late Devonian background state and its sensitivity to evolving external forcing across multiple models. In this context,

Earth System Models of Intermediate Complexity (EMICs) offer a promising path forward, as they allow for long-timescale simulations while explicitly resolving many key physical and biogeochemical processes.

## 5 Conclusions

We have explored the role of astronomical forcing in driving ocean anoxia under a Late Devonian climate configuration. Our experimental setup relies on an offline coupling between cGENIE and a fast climate–weathering emulator, based on a GCM, developed by Sablon et al. (2025). It allowed us to capture the influence of astronomical forcing on oceanic $[O_2]$ via its modulation of continental $PO_4$ weathering fluxes. At the global scale, astronomical forcing exerts a moderate impact on ocean $[O_2]$, with the most pronounced deoxygenation occurring during intervals of combined high eccentricity and high obliquity. While eccentricity and precession primarily affect $[O_2]$ through their control on $PO_4$ weathering fluxes, obliquity exerts its influence by modulating the insolation component of biological productivity at high latitudes, highlighting that even in a greenhouse world, obliquity can leave an imprint on ocean biogeochemistry, hence possibly sedimentary records. At the regional scale, eccentricity maxima also correspond to the most extensive anoxic conditions, providing new evidence supporting a strong impact of eccentricity maxima on the development of Late Devonian anoxic events. However, the biogeochemical response remains highly variable across regions. Our results show that astronomical forcing can act as a dominant control on ocean $[O_2]$, driving regional changes in anoxic volume of up to 19%. An unanticipated result is that local ocean circulation can represent a central driver of the spatial heterogeneity in $[O_2]$ responses to astronomical forcing. As a result, sedimentary records from different locations may reflect contrasting imprints of the same astronomical signal, potentially leading to contrasting interpretations of its role in pacing Late Devonian anoxia. Finally, while this study provides insights into how astronomical forcing affects Late Devonian ocean $[O_2]$, it also stresses the difficulty of explaining the duration of Devonian anoxic events and the uncertainties in their spatial extent, underscoring that much modelling and data integration work remains to fully understand the drivers and dynamics of Late Devonian anoxia.

### Appendix A: Background state and ocean circulation

Figure A1a, b, and d show a strong hemispheric asymmetry in oxygenation, with a substantially more oxygenated Northern Hemisphere compared to the Southern Hemisphere. This pattern primarily reflects large-scale ocean circulation (Fig. A1e), which allows well-oxygenated surface waters to ventilate the deep ocean in the Northern Hemisphere. In contrast, a pronounced oxygen minimum zone (OMZ) develops across much of the Southern Hemisphere (Fig. A1d), where meridional overturning circulation is nearly absent. The OMZ is shallower towards low latitudes, where primary productivity is high, consistent with enhanced biological oxygen demand (Fig. A1c). Primary productivity is also relatively elevated at high latitudes, while minimum values occur at mid latitudes, where downwelling associated with subtropical gyres prevents primary productivity. The seafloor $[O_2]$ map further indicates that most anoxic conditions at the seafloor are restricted to shallow ocean regions, as

confirmed by comparison with the model bathymetry (Fig. 1c). These shallow regions therefore correspond to areas where sedimentary P regeneration feedbacks are expected to be strongest.

Changes in ocean circulation associated with astronomical forcing are small in our simulations, with a maximum variation in overturning strength of 0.7 Sv (Sverdrup) when all orbital parameters vary together (0.56 Sv for eccentricity–precession forcing and 0.32 Sv for obliquity alone). Figure A2 further indicates that the main regions of deep-water formation remain largely unchanged between extreme orbital configurations (extracted from the 1.1 Myr transient simulation). Overall, the spatial distribution of deep-water formation explains the global overturning circulation pattern shown in Fig. A1e.

## Appendix B: Defining regions

This section clarifies how we refined the definition of the different regions based on the temporal variance of $[O_2]$ and $[PO_4]$. Figure B1 shows the normalized temporal variance of these two tracers, averaged over the upper 1000 m, consistent with the depth range applied in our regional analysis (see Section 3.2). First, a clear distinction between regions SA and WL emerges from both $[O_2]$ and $[PO_4]$ variance fields, particularly around 30°S and 60°W, providing strong justification for separating them. Second, region LG was initially split into two sub-regions based on the spatial structure of the variance fields. However, the temporal evolution and variability of $[O_2]$, anoxic volume, and $[PO_4]$ were found to be highly consistent across these sub-regions. Consequently, we merged them into a single, unified region, which we now refer to as region LG. These refinements provide a clear and consistent basis for the regional definitions presented in Fig. 4a. Although regional boundaries are somewhat arbitrary, they follow coherent patterns of variability and are broad enough to avoid overinterpreting hyper-localised phenomena (at the single grid cell level). The resulting regions are not intended as universal classifications, but rather as a practical framework for exploring the spatial heterogeneity of climate–biogeochemical interactions.

*Code availability.* The code for the version of the 'muffin' release of the cGENIE Earth system model used in this paper, is tagged as v0.9.50, and is assigned a DOI: *to be added*. Configuration files for the specific experiments presented in the paper can be found in the directory: *to be added*. Details of the experiments, plus the command line needed to run each one, are given in the 'readme.txt' file in that directory. All other configuration files and boundary conditions are provided as part of the code release. A manual detailing code installation, basic model configuration, tutorials covering various aspects of model configuration, experimental design, and output, plus the processing of results, is assigned the following DOI: https://doi.org/10.5281/zenodo.13377225. *Full directory and experiment information will be provided if the paper is accepted.*

*Video supplement.* Spatial $[O_2]$ anomaly (bottom), averaged from the second vertical layer down to approximately 1000 m depth, evolving through the 1.1 Myr astronomical solution (top). Dashed lines indicate the percentage of the water column (up to 1000 m) below the anoxic threshold of 6.5 $\mu$mol.kg$^{-1}$. The red dot represents climatic precession, the red cross eccentricity, and the blue dot obliquity. Periods of

reduced [$O_2$] appear as distinct pulses rather than a single prolonged event. For instance, severe deoxygenation is particularly evident at 0.15 and 0.98 Myr.

*Author contributions.* JG conducted the cGENIE experiments, developed the code for the analysis, performed all computations, and drafted the manuscript. AP contributed to the development of the open setup configuration of cGENIE. MC and ACDS contributed to the study design. All authors contributed to the discussion of results, writing the manuscript and approved the final version.

*Competing interests.* The contact author has declared that none of the authors has any competing interests.

*Acknowledgements.* This research is funded by the Belgian National Fund of Scientific Research (FNRS), project WarmAnoxia, PDR grant no. T.0037.22. Computational resources have been provided by the supercomputing facilities of the Université catholique de Louvain (CISM/UCL) and the Consortium des Équipements de Calcul Intensif en Fédération Wallonie Bruxelles (CÉCI). AP acknowledges the support of the French *Agence Nationale de la Recherche* (ANR) under reference ANR-23-CE01-0003 (project CYCLO-SED).

## References


Adloff, M., Ridgwell, A., Monteiro, F. M., Parkinson, I. J., Dickson, A., Pogge von Strandmann, P. A., Fantle, M. S., and Greene, S. E.: Inclusion of a suite of weathering tracers in the cGENIE Earth System Model–muffin release v. 0.9. 10, Geoscientific Model Development Discussions, 2020, 1–48, https://doi.org/https://doi.org/10.5194/gmd-14-4187-2021, 2020.

Algeo, T. J. and Scheckler, S. E.: Terrestrial-marine teleconnections in the Devonian: links between the evolution of land plants, weathering processes, and marine anoxic events, Philosophical Transactions of the Royal Society of London. Series B: Biological Sciences, 353, 113–130, https://doi.org/10.1098/rstb.1998.0195, 1998.

Becker, R., Marshall, J., Da Silva, A.-C., Agterberg, F., Gradstein, F., and Ogg, J.: The Devonian Period, in: Geologic Time Scale 2020, pp. 733–810, Elsevier, ISBN 978-0-12-824360-2, https://doi.org/10.1016/B978-0-12-824360-2.00022-X, 2020.

Benitez-Nelson, C. R.: The biogeochemical cycling of phosphorus in marine systems, Earth-Science Reviews, 51, 109–135, https://doi.org/https://doi.org/10.1016/S0012-8252(00)00018-0, 2000.

Berger, A. and Loutre, M. F.: Insolation values for the climate of the last 10 million years, Quaternary Science Reviews, 10, 297 – 317, https://doi.org/10.1016/0277-3791(91)90033-Q, 1991.

Bond, D. P. and Wignall, P. B.: The role of sea-level change and marine anoxia in the Frasnian–Famennian (Late Devonian) mass extinction, Palaeogeography, Palaeoclimatology, Palaeoecology, 263, 107–118, https://doi.org/https://doi.org/10.1016/j.palaeo.2008.02.015, 2008.

Bradley, J. A., Hülse, D., LaRowe, D. E., and Arndt, S.: Transfer efficiency of organic carbon in marine sediments, Nature communications, 13, 7297, https://doi.org/https://doi.org/10.1038/s41467-022-35112-9, 2022.

Bretherton, C. S., Widmann, M., Dymnikov, V. P., Wallace, J. M., and Bladé, I.: The effective number of spatial degrees of freedom of a time-varying field, Journal of climate, 12, 1990–2009, 1999.

Brugger, J., Hofmann, M., Petri, S., and Feulner, G.: On the Sensitivity of the Devonian Climate to Continental Configuration, Vegetation Cover, Orbital Configuration, $CO_2$ Concentration, and Insolation, Paleoceanography and Paleoclimatology, 34, 1375–1398, https://doi.org/10.1029/2019PA003562, 2019.

Cao, L., Eby, M., Ridgwell, A., Caldeira, K., Archer, D., Ishida, A., Joos, F., Matsumoto, K., Mikolajewicz, U., Mouchet, A., Orr, J. C., and Yool, A.: The role of ocean transport in the uptake of anthropogenic CO 2, Biogeosciences, 6, 375–390, https://doi.org/10.5194/bg-6-375-2009, 2009.

Carmichael, S. K., Waters, J. A., Königshof, P., Suttner, T. J., and Kido, E.: Paleogeography and paleoenvironments of the Late Devonian Kellwasser event: A review of its sedimentological and geochemical expression, Global and Planetary Change, 183, 102 984, https://doi.org/10.1016/j.gloplacha.2019.102984, 2019.

Cermeño, P., García-Comas, C., Pohl, A., Williams, S., Benton, M. J., Chaudhary, C., Le Gland, G., Müller, R. D., Ridgwell, A., and Vallina, S. M.: Post-extinction recovery of the Phanerozoic oceans and biodiversity hotspots, Nature, 607, 507–511, https://www.nature.com/articles/s41586-022-04932-6, 2022.

Chen, B., Ma, X., Mills, B. J., Qie, W., Joachimski, M. M., Shen, S., Wang, C., Xu, H., and Wang, X.: Devonian paleoclimate and its drivers: A reassessment based on a new conodont $\delta$18O record from South China, Earth-Science Reviews, 222, 103 814, https://doi.org/https://doi.org/10.1016/j.earscirev.2021.103814, 2021.

Chen, D., Wang, J., Racki, G., Li, H., Wang, C., Ma, X., and Whalen, M. T.: Large sulphur isotopic perturbations and oceanic changes during the Frasnian–Famennian transition of the Late Devonian, Journal of the Geological Society, 170, 465–476, https://doi.org/10.1144/jgs2012-037, 2013.

Claussen, M., Mysak, L., Weaver, A., Crucifix, M., Fichefet, T., Loutre, M.-F., Weber, S., Alcamo, J., Alexeev, V., Berger, A., Calov, R., Ganopolski, A., Goosse, H., Lohmann, G., Lunkeit, F., Mokhov, I., Petoukhov, V., Stone, P., and Wang, Z.: Earth system models of intermediate complexity: closing the gap in the spectrum of climate system models, Climate Dynamics, 18, 579–586, https://doi.org/10.1007/s00382-001-0200-1, 2002.

Colbourn, G., Ridgwell, A., and Lenton, T.: The rock geochemical model (RokGeM) v0. 9, Geoscientific Model Development, 6, 1543–1573, 2013.

Crichton, K. A., Wilson, J. D., Ridgwell, A., and Pearson, P. N.: Calibration of temperature-dependent ocean microbial processes in the cGENIE.muffin (v0.9.13) Earth system model, Geoscientific Model Development, 14, 125–149, https://doi.org/10.5194/gmd-14-125-2021, 2021.

Crucifix, M.: Generation of sample climatic precession and obliquity solutions for running climate experiments over the Devonian, https://doi.org/10.5281/zenodo.14894811, 2025.

Da Silva, A.-C., Sinnesael, M., Claeys, P., Davies, J. H. F. L., De Winter, N. J., Percival, L. M. E., Schaltegger, U., and De Vleeschouwer, D.: Anchoring the Late Devonian mass extinction in absolute time by integrating climatic controls and radio-isotopic dating, Scientific Reports, 10, 12 940, https://doi.org/10.1038/s41598-020-69097-6, 2020.

Dahl, T. W., Harding, M. A., Brugger, J., Feulner, G., Norrman, K., Lomax, B. H., and Junium, C. K.: Low atmospheric CO2 levels before the rise of forested ecosystems, Nature Communications, 13, 7616, https://doi.org/https://doi.org/10.1038/s41467-022-35085-9, 2022.

De Vleeschouwer, D., Da Silva, A.-C., Boulvain, F., Crucifix, M., and Claeys, P.: Precessional and half-precessional climate forcing of Mid-Devonian monsoon-like dynamics, Climate of the Past, 8, 337–351, https://doi.org/https://doi.org/10.5194/cp-8-337-2012, 2012.

De Vleeschouwer, D., Rakociński, M., Racki, G., Bond, D. P., Sobień, K., and Claeys, P.: The astronomical rhythm of Late-Devonian climate change (Kowala section, Holy Cross Mountains, Poland), Earth and Planetary Science Letters, 365, 25–37, https://doi.org/10.1016/j.epsl.2013.01.016, 2013.

De Vleeschouwer, D., Crucifix, M., Bounceur, N., and Claeys, P.: The impact of astronomical forcing on the Late Devonian greenhouse climate, Global and Planetary Change, 120, 65–80, https://doi.org/10.1016/j.gloplacha.2014.06.002, 2014.

De Vleeschouwer, D., Da Silva, A.-C., Sinnesael, M., Chen, D., Day, J. E., Whalen, M. T., Guo, Z., and Claeys, P.: Timing and pacing of the Late Devonian mass extinction event regulated by eccentricity and obliquity, Nature Communications, 8, 2268, https://doi.org/10.1038/s41467-017-02407-1, 2017.

Dopieralska, J.: Reconstructing seawater circulation on the Moroccan shelf of Gondwana during the Late Devonian: Evidence from Nd isotope composition of conodonts, Geochemistry, Geophysics, Geosystems, 10, https://doi.org/10.1029/2008GC002247, 2009.

Dunne, J. P., Sarmiento, J. L., and Gnanadesikan, A.: A synthesis of global particle export from the surface ocean and cycling through the ocean interior and on the seafloor, Global Biogeochemical Cycles, 21, https://doi.org/https://doi.org/10.1029/2006GB002907, 2007.

Edwards, N. R. and Marsh, R.: Uncertainties due to transport-parameter sensitivity in an efficient 3-D ocean-climate model, Climate Dynamics, 24, 415–433, https://doi.org/10.1007/s00382-004-0508-8, 2005.

Farhat, M., Auclair-Desrotour, P., Boué, G., and Laskar, J.: The resonant tidal evolution of the Earth-Moon distance, Astronomy & Astrophysics, 665, L1, https://doi.org/10.1051/0004-6361/202243445, publisher: EDP Sciences, 2022.

Frankignoulle, M. and Gattuso, J.-P.: Air-sea CO2 exchange in coastal ecosystems, in: Interactions of C, N, P and S biogeochemical cycles and global change, pp. 233–248, Springer, https://doi.org/https://doi.org/10.1007/978-3-642-76064-8_9, 1993.

Garcia, H. E., Wang, Z., Bouchard, C., Cross, S. L., Paver, C. R., Reagan, J. R., Boyer, T. P., Locarnini, R. A., Mishonov, A. V., Baranova, O. K., et al.: World Ocean Atlas 2023, Volume 3: Dissolved Oxygen, Apparent Oxygen Utilization, Dissolved Oxygen Saturation and 30-year Climate Normal, https://doi.org/https://doi.org/10.25923/rb67-ns53, 2024.

Gough, D.: Solar interior structure and luminosity variations, in: Physics of Solar Variations: Proceedings of the 14th ESLAB Symposium held in Scheveningen, The Netherlands, 16–19 September, 1980, pp. 21–34, Springer, 1981.

Granot, R.: Palaeozoic oceanic crust preserved beneath the eastern Mediterranean, Nature Geoscience, 9, 701–705, https://doi.org/https://doi.org/10.1038/ngeo2784, 2016.

Gérard, J. and Crucifix, M.: Diagnosing the causes of AMOC slowdown in a coupled model: a cautionary tale, Earth System Dynamics, 15, 293–306, https://doi.org/10.5194/esd-15-293-2024, 2024.

Gérard, J., Sablon, L., Huygh, J. J. C., Da Silva, A.-C., Pohl, A., Vérard, C., and Crucifix, M.: Exploring the mechanisms of Devonian oceanic anoxia: impact of ocean dynamics, palaeogeography, and orbital forcing, Climate of the Past, 21, 239–260, https://doi.org/10.5194/cp-21-239-2025, 2025.

Haddad, E. E., Boyer, D. L., Droser, M. L., Lee, B. K., Lyons, T. W., and Love, G. D.: Ichnofabrics and chemostratigraphy argue against persistent anoxia during the Upper Kellwasser Event in New York State, Palaeogeography, Palaeoclimatology, Palaeoecology, 490, 178–190, https://doi.org/10.1016/j.palaeo.2017.10.025, 2018.

Hedhli, M., Grasby, S., Henderson, C., and Davis, B.: Multiple diachronous “Black Seas” mimic global ocean anoxia during the latest Devonian, Geology, 51, 973–977, https://doi.org/10.1130/G51394.1, 2023.

Huang, C., Joachimski, M. M., and Gong, Y.: Did climate changes trigger the Late Devonian Kellwasser Crisis? Evidence from a high-resolution conodont $\delta$18OPO4 record from South China, Earth and Planetary Science Letters, 495, 174–184, https://doi.org/https://doi.org/10.1016/j.epsl.2018.05.016, 2018.

Hülse, D. and Ridgwell, A.: Instability in the geological regulation of Earth’s climate, Science, 389, eadh7730, https://doi.org/10.1126/science.adh7730, 2025.

Hülse, D., Arndt, S., Daines, S., Regnier, P., and Ridgwell, A.: OMEN-SED 1.0: a novel, numerically efficient organic matter sediment diagenesis module for coupling to Earth system models, Geoscientific Model Development, 11, 2649–2689, https://doi.org/https://doi.org/10.5194/gmd-11-2649-2018, 2018.

Huygh, J. J. C., Algeo, T. J., Sageman, B. B., Arts, M. C., Ver Straeten, C. A., Over, D. J., Gérard, J., Sablon, L., Crucifix, M., and Da Silva, A.-C.: Astronomical control on marine anoxia during the Kellwasser Crisis and Rhinestreet Event (Appalachian Basin, New York, USA), 2025.

Ingall, E. and Jahnke, R.: Evidence for enhanced phosphorus regeneration from marine sediments overlain by oxygen depleted waters, Geochimica et Cosmochimica Acta, 58, 2571–2575, https://doi.org/https://doi.org/10.1016/0016-7037(94)90033-7, 1994.

Joachimski, M. M. and Buggisch, W.: Conodont apatite $\delta$18O signatures indicate climatic cooling as a trigger of the Late Devonian mass extinction, Geology, 30, 711–714, https://doi.org/https://doi.org/10.1130/0091-7613(2002)030<0711:CAOSIC>2.0.CO;2, 2002.

Kabanov, P., Hauck, T. E., Gouwy, S. A., Grasby, S. E., and Van Der Boon, A.: Oceanic anoxic events, photic-zone euxinia, and controversy of sea-level fluctuations during the Middle-Late Devonian, Earth-Science Reviews, 241, 104 415, https://doi.org/10.1016/j.earscirev.2023.104415, 2023.

Kaiser, S. I., Aretz, M., and Becker, R. T.: The global Hangenberg Crisis (Devonian–Carboniferous transition): review of a first-order mass extinction, Geological Society, London, Special Publications, 423, 387–437, https://doi.org/10.1144/SP423.9, 2016.

Kiessling, W., Flügel, E., and Golonka, J.: Patterns of Phanerozoic carbonate platform sedimentation, Lethaia, 36, 195–226, https://doi.org/https://doi.org/10.1080/00241160310004648, 2003.

Krause, A. J., Mills, B. J., Zhang, S., Planavsky, N. J., Lenton, T. M., and Poulton, S. W.: Stepwise oxygenation of the Paleozoic atmosphere, Nature Communications, 9, 4081, https://doi.org/https://doi.org/10.1038/s41467-018-06383-y, 2018.

Laridon, A., Couplet, V., Gérard, J., Thiery, W., and Crucifix, M.: Connecting complex and simplified models of tipping elements: a nonlinear two-forcing emulator for the Atlantic meridional overturning circulation, Open Research Europe, 5, 87, 2025.

Laskar, J. and Robutel, P.: The chaotic obliquity of the planets, Nature, 361, 608–612, https://doi.org/10.1038/361608a0, 1993.

Laskar, J., Robutel, P., Joutel, F., Gastineau, M., Correia, A. C., and Levrard, B.: A long-term numerical solution for the insolation quantities of the Earth, Astronomy & Astrophysics, 428, 261–285, https://doi.org/https://doi.org/10.1051/0004-6361:20041335, 2004.

Laskar, J., Fienga, A., Gastineau, M., and Manche, H.: La2010: a new orbital solution for the long-term motion of the Earth, Astronomy and Astrophysics, 532, A89, https://doi.org/10.1051/0004-6361/201116836, 2011.

Lunt, D., Williamson, M., Valdes, P., Lenton, T., and Marsh, R.: Comparing transient, accelerated, and equilibrium simulations of the last 30 000 years with the GENIE-1 model, Climate of the Past, 2, 221–235, https://doi.org/10.5194/cp-2-221-2006, 2006.

Ma, K., Hinnov, L., Zhang, X., and Gong, Y.: Astronomical climate changes trigger Late Devonian bio-and environmental events in South China, Global and Planetary Change, 215, 103 874, https://doi.org/https://doi.org/10.1016/j.gloplacha.2022.103874, 2022.

Ma, X., Gong, Y., Chen, D., Racki, G., Chen, X., and Liao, W.: The Late Devonian Frasnian–Famennian Event in South China—patterns and causes of extinctions, sea level changes, and isotope variations, Palaeogeography, Palaeoclimatology, Palaeoecology, 448, 224–244, https://doi.org/https://doi.org/10.1016/j.palaeo.2015.10.047, 2016.

Maffre, P., Goddéris, Y., Le Hir, G., Nardin, É., Sarr, A.-C., and Donnadieu, Y.: GEOCLIM7, an Earth system model for multi-million-year evolution of the geochemical cycles and climate, Geoscientific Model Development, 18, 6367–6413, https://doi.org/https://doi.org/10.5194/gmd-18-6367-2025, 2025.

Marsh, R., Müller, S. A., Yool, A., and Edwards, N. R.: Incorporation of the C-GOLDSTEIN efficient climate model into the GENIE framework: "eb_go_gs" configurations of GENIE, Geoscientific Model Development, 4, 957–992, https://doi.org/10.5194/gmd-4-957-2011, 2011.

Marsh, R., Sobester, A., Hart, E. E., Oliver, K., Edwards, N., and Cox, S.: An optimally tuned ensemble of the" eb_go_gs" configuration of GENIE: parameter sensitivity and bifurcations in the Atlantic overturning circulation, Geoscientific Model Development Discussions, 6, 925–956, https://doi.org/10.5194/gmd-6-1729-2013, 2013.

Martinez, M. and Dera, G.: Orbital pacing of carbon fluxes by a 9-My eccentricity cycle during the Mesozoic, Proceedings of the National Academy of Sciences, 112, 12 604–12 609, https://doi.org/https://doi.org/10.1073/pnas.1419946112, 2015.

Mills, B. J., Krause, A. J., Jarvis, I., and Cramer, B. D.: Evolution of atmospheric O2 through the Phanerozoic, revisited, Annual review of earth and planetary sciences, 51, 253–276, 2023.

Naidoo-Bagwell, A. A., Monteiro, F. M., Hendry, K. R., Burgan, S., Wilson, J. D., Ward, B. A., Ridgwell, A., and Conley, D. J.: A diatom extension to the cGEnIE Earth system model–EcoGEnIE 1.1, Geoscientific Model Development, 17, 1729–1748, https://doi.org/https://doi.org/10.5194/gmd-17-1729-2024, 2024.

Paschall, O., Carmichael, S. K., Königshof, P., Waters, J. A., Ta, P. H., Komatsu, T., and Dombrowski, A.: The Devonian-Carboniferous boundary in Vietnam: Sustained ocean anoxia with a volcanic trigger for the Hangenberg Crisis?, Global and Planetary Change, 175, 64–81, https://doi.org/10.1016/j.gloplacha.2019.01.021, 2019.

Percival, L., Bond, D., Rakociński, M., Marynowski, L., Hood, A., Adatte, T., Spangenberg, J., and Föllmi, K.: Phosphorus-cycle disturbances during the Late Devonian anoxic events, Global and Planetary Change, 184, 103 070, https://doi.org/10.1016/j.gloplacha.2019.103070, 2020.

Pier, J. Q., Brisson, S. K., Beard, J. A., Hren, M. T., and Bush, A. M.: Accelerated mass extinction in an isolated biota during Late Devonian climate changes, Scientific Reports, 11, 24 366, https://doi.org/https://doi.org/10.1038/s41598-021-03510-6, 2021.

Pohl, A., Ridgwell, A., Stockey, R. G., Thomazo, C., Keane, A., Vennin, E., and Scotese, C. R.: Continental configuration controls ocean oxygenation during the Phanerozoic, Nature, 608, 523–527, https://doi.org/10.1038/s41586-022-05018-z, 2022.

Racki, G.: A volcanic scenario for the Frasnian–Famennian major biotic crisis and other Late Devonian global changes: more answers than questions?, Global and Planetary Change, 189, 103 174, https://doi.org/https://doi.org/10.1016/j.gloplacha.2020.103174, 2020.

Rahmstorf, S., Crucifix, M., Ganopolski, A., Goosse, H., Kamenkovich, I., Knutti, R., Lohmann, G., Marsh, R., Mysak, L. A., Wang, Z., and Weaver, A. J.: Thermohaline circulation hysteresis: A model intercomparison, Geophysical Research Letters, 32, 2005GL023 655, https://doi.org/10.1029/2005GL023655, 2005.

Reershemius, T. and Planavsky, N. J.: What controls the duration and intensity of ocean anoxic events in the Paleozoic and the Mesozoic?, Earth-Science Reviews, 221, 103 787, https://doi.org/https://doi.org/10.1016/j.earscirev.2021.103787, 2021.

Reinhard, C. T., Olson, S. L., Kirtland Turner, S., Pälike, C., Kanzaki, Y., and Ridgwell, A.: Oceanic and atmospheric methane cycling in the cGENIE Earth system model – release v0.9.14, Geoscientific Model Development, 13, 5687–5706, https://doi.org/10.5194/gmd-13-5687-2020, 2020.

Ridgwell, A.: A Mid Mesozoic Revolution in the regulation of ocean chemistry, Marine Geology, 217, 339–357, https://doi.org/https://doi.org/10.1016/j.margeo.2004.10.036, 2005.

Ridgwell, A.: derpycode/muffingen: v0.9.24, https://doi.org/10.5281/zenodo.7545809, 2023.

Ridgwell, A. and Hargreaves, J.: Regulation of atmospheric CO2 by deep-sea sediments in an Earth system model, Global Biogeochemical Cycles, 21, https://doi.org/https://doi.org/10.1029/2006GB002764, 2007.

Ridgwell, A., Hargreaves, J., Edwards, N. R., Annan, J., Lenton, T. M., Marsh, R., Yool, A., and Watson, A.: Marine geochemical data assimilation in an efficient Earth System Model of global biogeochemical cycling, Biogeosciences, 4, 87–104, https://doi.org/10.5194/bg-4-87-2007, 2007.

Ruttenberg, K.: The global phosphorus cycle, Treatise on geochemistry, 8, 585–643, https://doi.org/https://doi.org/10.1016/B0-08-043751-6/08153-6, 2003.

Sablon, L., Maffre, P., Goddéris, Y., Valdes, P. J., Gérard, J., Huygh, J. J. C., Da Silva, A.-C., and Crucifix, M.: An Emulator-Based Modelling Framework for Studying Astronomical Controls on Ocean Anoxia with an Application on the Devonian, EGUsphere, 2025, 1–36, https://doi.org/10.5194/egusphere-2025-1696, 2025.

Sarr, A., Donnadieu, Y., Laugié, M., Ladant, J., Suchéras-Marx, B., and Raisson, F.: Ventilation Changes Drive Orbital-Scale Deoxygenation Trends in the Late Cretaceous Ocean, Geophysical Research Letters, 49, e2022GL099 830, https://doi.org/10.1029/2022GL099830, 2022.

Schmidtko, S., Stramma, L., and Visbeck, M.: Decline in global oceanic oxygen content during the past five decades, Nature, 542, 335–339, https://doi.org/https://doi.org/10.1038/nature21399, 2017.

Scotese, C. R. and Wright, N.: PALEOMAP paleodigital elevation models (PaleoDEMS) for the Phanerozoic, Paleomap Proj, https://doi.org/https://doi.org/10.5281/zenodo.5348492, 2018.

Sharaf, S. G. and Boudnikova, N. A.: Secular variations of elements of the Earth's orbit which influences the climates of the geological past, Tr. Inst. Theor. Astron. Leningrad, 11, 231–261, 1967.

Sharoni, S. and Halevy, I.: Rates of seafloor and continental weathering govern Phanerozoic marine phosphate levels, Nature geoscience, 16, 75–81, https://doi.org/https://doi.org/10.1038/s41561-022-01075-1, 2023.

Smart, M. S., Filippelli, G., Gilhooly, W. P., Ozaki, K., Reinhard, C. T., Marshall, J. E. A., and Whiteside, J. H.: The Expansion of Land Plants during the Late Devonian Contributed to the Marine Mass Extinction, Communications Earth & Environment, 4, 1–13, https://doi.org/10.1038/s43247-023-01087-8, 2023.

Song, H., Song, H., Algeo, T. J., Tong, J., Romaniello, S. J., Zhu, Y., Chu, D., Gong, Y., and Anbar, A. D.: Uranium and carbon isotopes document global-ocean redox-productivity relationships linked to cooling during the Frasnian-Famennian mass extinction, Geology, 45, 887–890, https://doi.org/10.1130/G39393.1, 2017.

Stappard, D. A., Wilson, J. D., Yool, A., and Tyrrell, T.: NutGEnIE 1.0: nutrient cycle extensions to the cGEnIE Earth system model to examine the long-term influence of nutrients on oceanic primary production, EGUsphere, 2025, 1–33, https://doi.org/https://doi.org/10.5194/egusphere-2025-436, 2025.

Tostevin, R. and Mills, B. J.: Reconciling proxy records and models of Earth's oxygenation during the Neoproterozoic and Palaeozoic, Interface focus, 10, 20190 137, https://doi.org/https://doi.org/10.1098/rsfs.2019.0137, 2020.

Valdes, P. J., Armstrong, E., Badger, M. P. S., Bradshaw, C. D., Bragg, F., Crucifix, M., Davies-Barnard, T., Day, J. J., Farnsworth, A., Gordon, C., Hopcroft, P. O., Kennedy, A. T., Lord, N. S., Lunt, D. J., Marzocchi, A., Parry, L. M., Pope, V., Roberts, W. H. G., Stone, E. J., Tourte, G. J. L., and Williams, J. H. T.: The BRIDGE HadCM3 Family of Climate Models: HadCM3@Bristol v1.0, Geoscientific Model Development, 10, 3715–3743, https://doi.org/10.5194/gmd-10-3715-2017, 2017.

Valdes, P. J., Scotese, C. R., and Lunt, D. J.: Deep ocean temperatures through time, Climate of the Past Discussions, 2021, 1–37, https://doi.org/https://doi.org/10.5194/cp-17-1483-2021, 2020.

Van De Velde, S. J., Hülse, D., Reinhard, C. T., and Ridgwell, A.: Iron and sulfur cycling in the cGENIE.muffin Earth system model (v0.9.21), Geoscientific Model Development, 14, 2713–2745, https://doi.org/10.5194/gmd-14-2713-2021, 2021.

Vervoort, P., Kirtland Turner, S., Rochholz, F., and Ridgwell, A.: Earth system model analysis of how astronomical forcing is imprinted onto the marine geological record: The role of the inorganic (carbonate) carbon cycle and feedbacks, Paleoceanography and Paleoclimatology, 39, e2023PA004 826, https://doi.org/https://doi.org/10.1029/2023PA004826, 2024.

Vérard, C.: Panalesis: towards global synthetic palaeogeographies using integration and coupling of manifold models, Geological Magazine, 156, 320–330, https://doi.org/10.1017/S0016756817001042, 2019.

Wallmann, K.: Phosphorus imbalance in the global ocean?, Global Biogeochemical Cycles, 24, https://doi.org/https://doi.org/10.1029/2009GB003643, 2010.

Ward, B. A., Wilson, J. D., Death, R. M., Monteiro, F. M., Yool, A., and Ridgwell, A.: EcoGEnIE 1.0: plankton ecology in the cGEnIE Earth system model, Geoscientific Model Development, 11, 4241–4267, https://doi.org/10.5194/gmd-11-4241-2018, 2018.

Wichern, N. M. A., Bialik, O. M., Nohl, T., Percival, L. M. E., Becker, R. T., Kaskes, P., Claeys, P., and De Vleeschouwer, D.: Astronomically paced climate and carbon cycle feedbacks in the lead-up to the Late Devonian Kellwasser Crisis, Climate of the Past, 20, 415–448, https://doi.org/10.5194/cp-20-415-2024, 2024.

Wilde, P. and Berry, W.: Destabilization of the oceanic density structure and its significance to marine "extinction" events, Palaeogeography, Palaeoclimatology, Palaeoecology, 48, 143–162, https://doi.org/https://doi.org/10.1016/0031-0182(84)90041-5, 1984.

Zeebe, R. E. and Lantink, M. L.: A Secular Solar System Resonance that Disrupts the Dominant Cycle in EarthÔÇÖs Orbital Eccentricity (g 2 ÔêÆ g 5): Implications for Astrochronology, The Astronomical Journal, 167, 204, https://doi.org/10.3847/1538-3881/ad32cf, 2024.

Zelinka, M. D., Myers, T. A., McCoy, D. T., Po-Chedley, S., Caldwell, P. M., Ceppi, P., Klein, S. A., and Taylor, K. E.: Causes of higher climate sensitivity in CMIP6 models, Geophysical Research Letters, 47, e2019GL085 782, https://doi.org/https://doi.org/10.1029/2019GL085782, 2020.

Šidlichovský, M. and Nesvorný, D.: Frequency Modified Fourier Transform and its Application to Asteroids, The Dynamical Behaviour of our Planetary System, p. 137–148, https://doi.org/10.1007/978-94-011-5510-6_9, 1997.

| Name | Type | Emulator | Duration (kyr) | IC | Forcings | BC |
|---|---|---|---|---|---|---|
| SPIN1 | Closed | Off | 20 | — | $pCO_2$; $pO_2$; surface flux of DIC and ALK | Constant wind fields and albedo profile (HadCM3L) |
| SPIN2 | Open | Off | 500 | SPIN1 | $pO_2$ | as in SPIN1 |
| SPIN3 | Open | On | 100 | SPIN2 | $pO_2$ | as in SPIN1 |
| Full | Open | On | 1100 | SPIN3 | $pO_2$ | as in SPIN1 |
| Obli | Open | On | 1100 | SPIN3 | $pO_2$ | as in SPIN1 |
| Ecc-prec | Open | On | 1100 | SPIN3 | $pO_2$ | as in SPIN1 |

**Table 1. Experimental design.** The type indicates whether the model operates in a closed or open configuration, with the closed setup meaning that every chemical species lost through sedimentation is compensated by an equivalent input from weathering. The emulator is the one from Sablon et al. (2025) that is built on model outputs from HadCM3L, HadSM3, and GEOCLIM. Initial conditions (IC) for SPIN1 are derived from GEOCLIM simulations and include $PO_4$, alkalinity (ALK), calcium, and sulfate. Forcings correspond to quantities that are explicitly prescribed during the simulations and are the same as in Hülse and Ridgwell (2025). Boundary conditions (BC) are derived from HadCM3L simulations as described in Valdes et al. (2020).

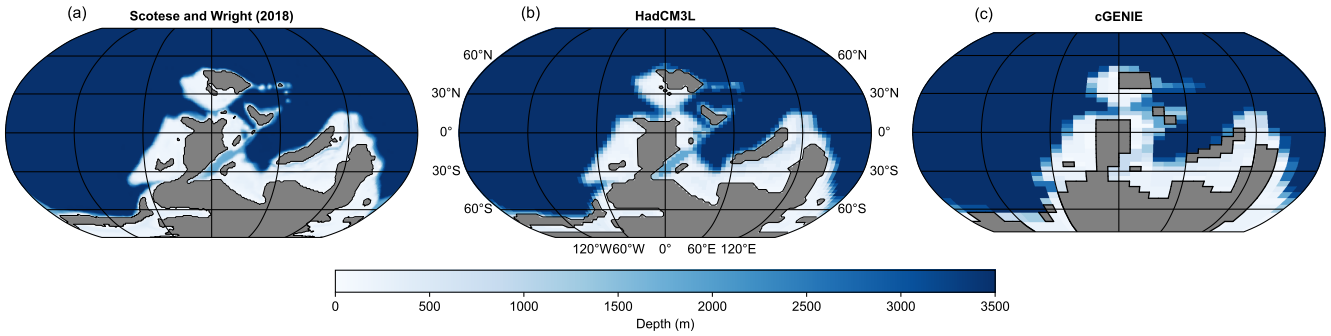


**Figure 1. Late Devonian (370 Ma) bathymetry**. Comparison between **(a)** the continental reconstruction from Scotese and Wright (2018), **(b)** the same reconstruction interpolated onto the HadCM3L model grid used in the emulator and **(c)** as per **(b)** on the cGENIE grid.

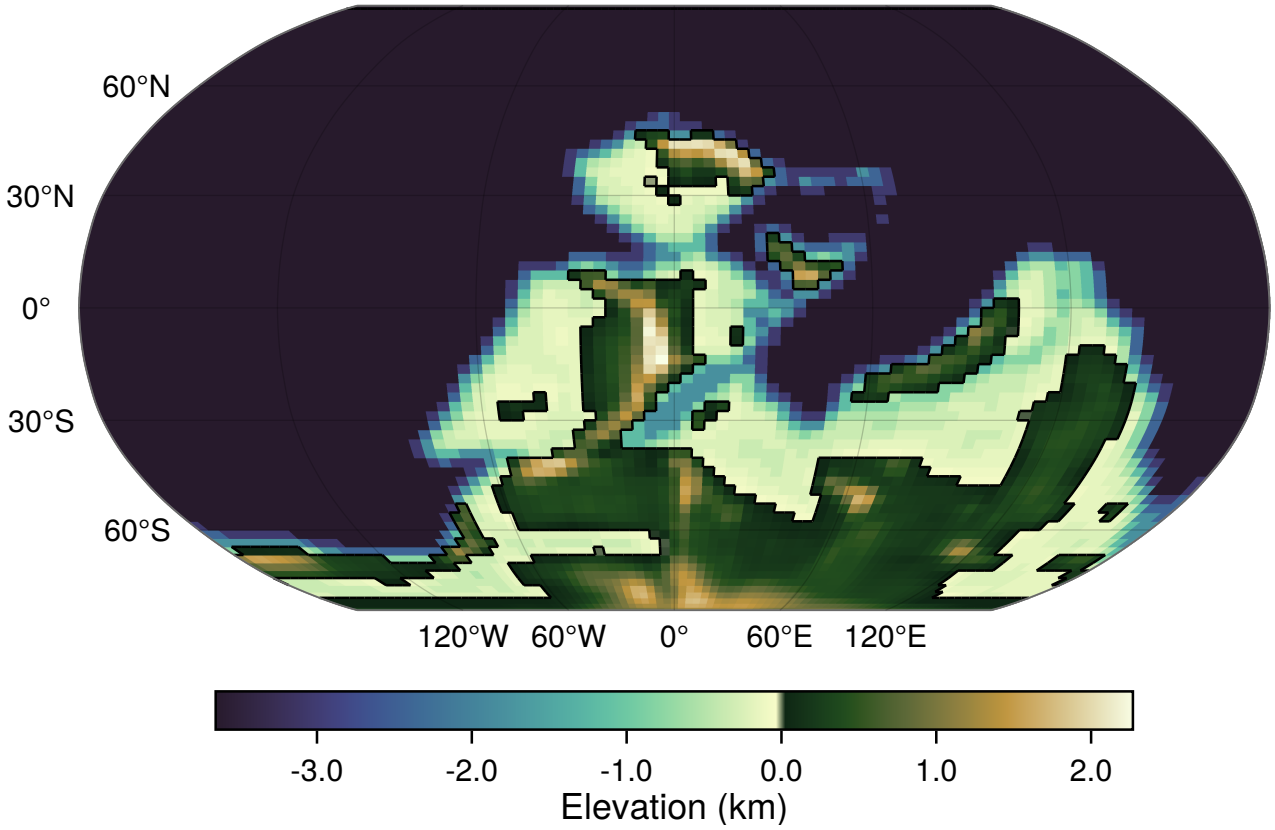


**Figure 2. Topography of the Late Devonian (370 Ma)**. Topography according to Scotese and Wright (2018), reproduced from Sablon et al. (2025). The bathymetry is identical to the one shown in Fig. 1b.

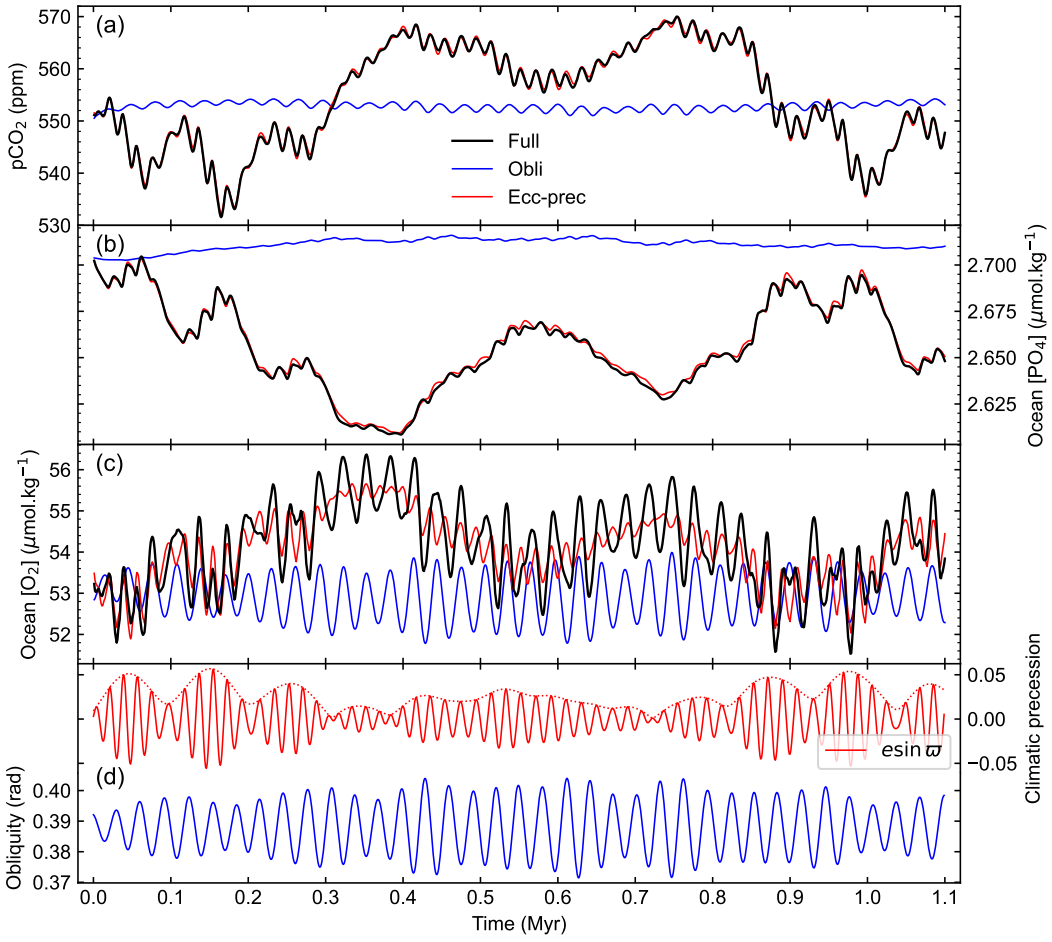


**Figure 3. Global response to astronomical forcing**. Global time series of **(a)** $pCO_2$, ocean **(b)** $[PO_4]$ and **(c)** $[O_2]$. The black curve represents the simulation in which all astronomical parameters evolve. The blue curve represents the simulation with only obliquity varying, while the red curve corresponds to the simulation where only eccentricity and precession evolve. **(d)** The astronomical solution used in the simulations, with eccentricity in dotted red, climatic precession in red and obliquity in blue. Here, $e$ denotes the eccentricity, and $\varpi$ represents the longitude of perihelion.

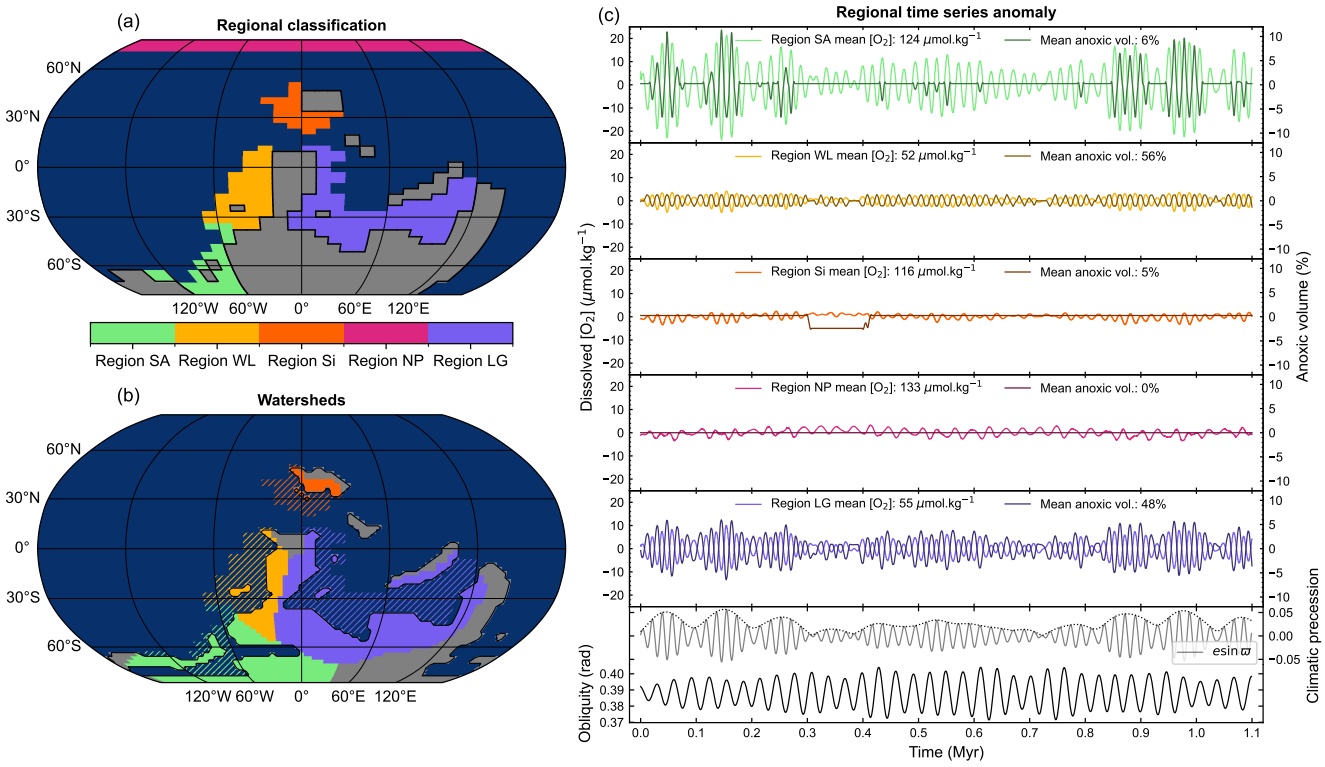


**Figure 4. Regional variation of [$O_2$] and anoxia**. **(a)** Definition of the five regions. **(b)** Watersheds based on the nearest-neighbour continental runoff routing scheme. The colour of the continental grid cell indicates in which region the weathering flux of $PO_4$ computed by the emulator of Sablon et al. (2025) is routed. The hashed areas represent the regions as defined in cGENIE and are the same as in panel **(a)**. The discrepancies between the watersheds and the regions arise from the different grid resolution of cGENIE and HadSM3. **(c)** Time series of average oceanic [$O_2$] anomalies and anoxic volume anomalies (in %) for each region. These quantities were computed over the full extent of each region, from the second vertical layer down to approximately 1000 m depth, excluding the surface layer as it is in equilibrium with the atmosphere. The anoxic volume is shown in a darker colour, and the anomaly is expressed as a difference of %. The anoxic threshold is set at 6.5 $\mu$mol.kg$^{-1}$ after Sarr et al. (2022). For both [$O_2$] and anoxic volume, the y-axis scales are identical across all regional panels to allow direct comparison. As in Fig. 3, the bottom panel displays the astronomical forcing, but shown in black for clarity.

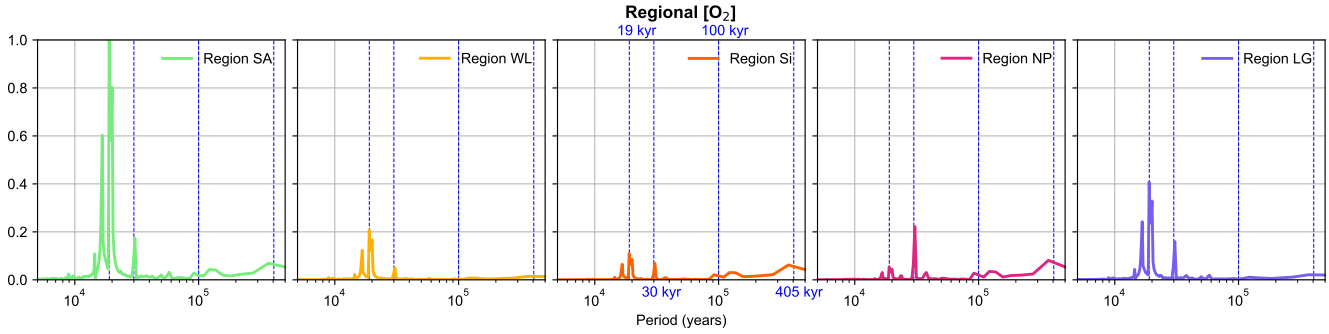


**Figure 5. Normalized Fourier power spectrum of the regional [$O_2$] time series**. Vertical dashed lines indicate the characteristic periods of the astronomical parameters: 19 kyr for precession, 30 kyr for obliquity, and 100 kyr and 405 kyr for eccentricity.

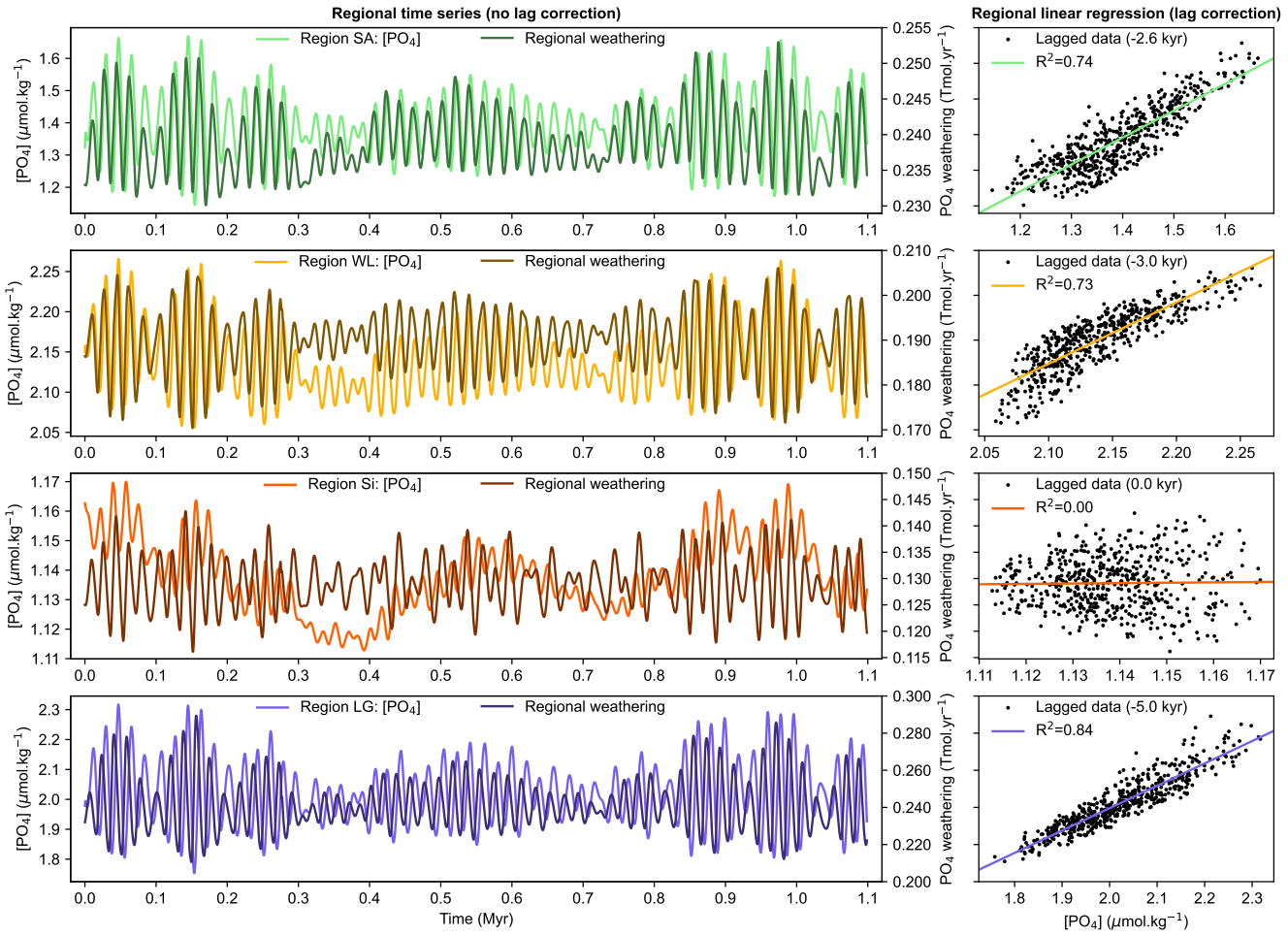


**Figure 6. Link between continental $PO_4$ weathering flux and regional [$PO_4$].** Displayed are correlations between regional [$PO_4$] and their corresponding regional weathering fluxes. A negative time lag is applied in the figures on the right, where the regression is computed, and is absent from the figures on the left. Regions SA, WL, and LG have all p-values smaller than $10^{-3}$, while region Si has a p-value of 0.35. Region NP is excluded from the analysis due to the absence of direct continental $PO_4$ weathering.

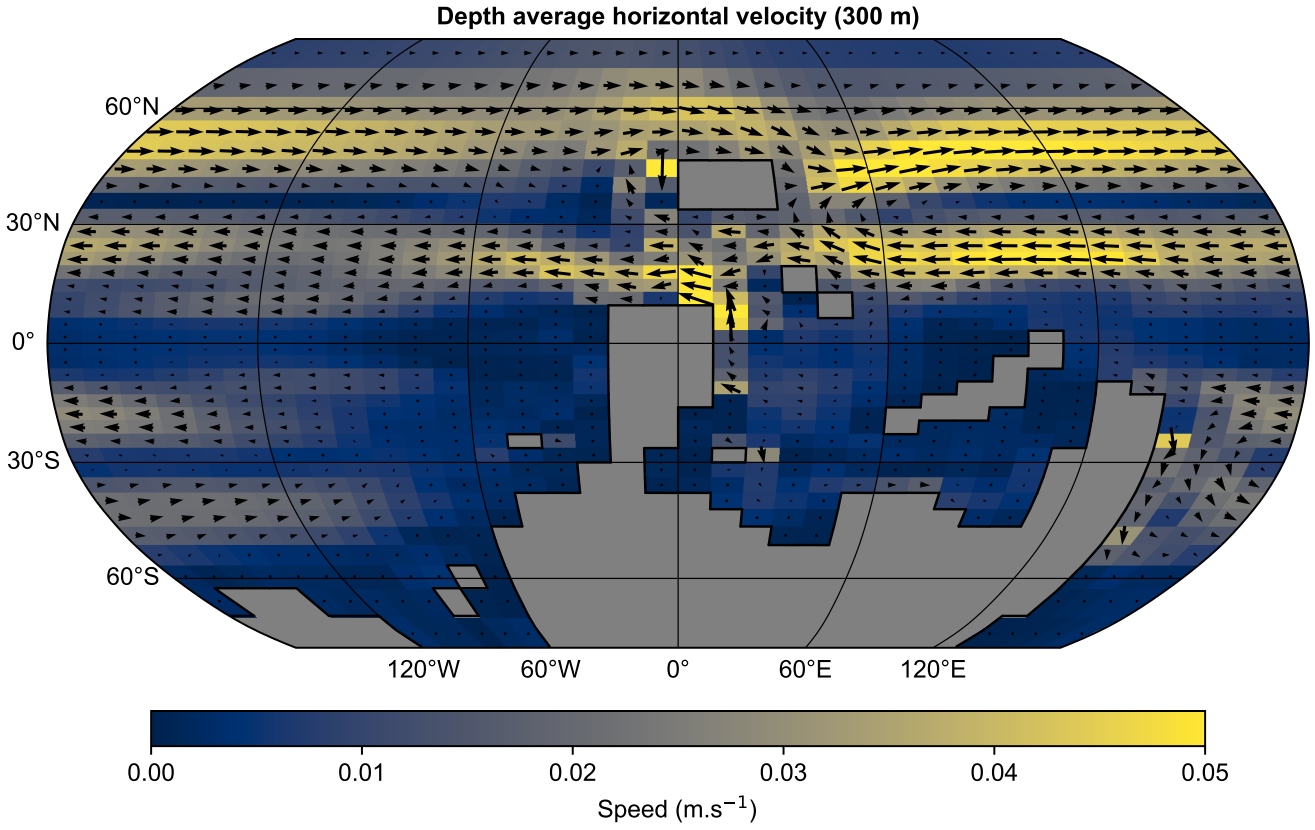


**Figure 7. Surface ocean circulation**. Mean horizontal ocean velocity (m.s$^{-1}$) averaged over the upper 300 m. Arrow direction indicates flow orientation, while arrow length is proportional to velocity magnitude (also represented with background shading).

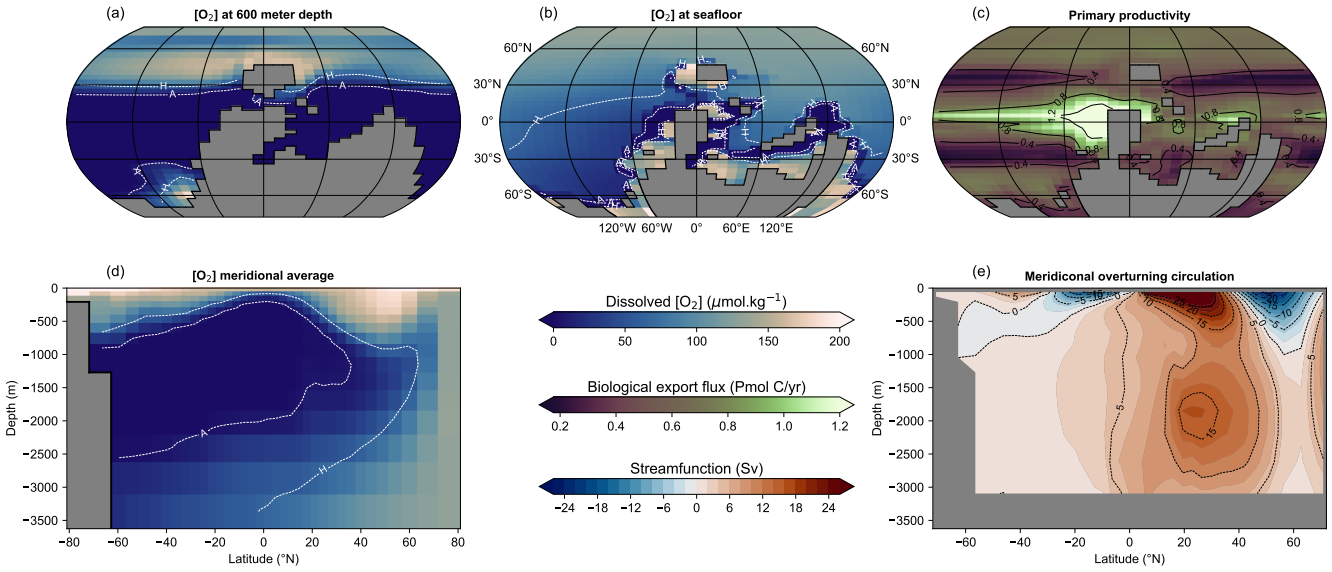


**Figure A1. Background state at the end of SPIN3.** [$O_2$] at a depth of 600m **(a)** and at the seafloor **(b)**. **(c)** Primary productivity (Pmol C $yr^{-1}$). **(d)** Meridional average of [$O_2$]. **(e)** Meridional overturning streamfunction (1 Sv $\equiv 10^6$ $m^3$ $s^{-1}$). The white dashed lines in **(a)**, **(b)**, and **(d)** indicate the boundaries for the anoxic (A) and hypoxic (H) regions, with threshold values taken after Sarr et al. (2022).

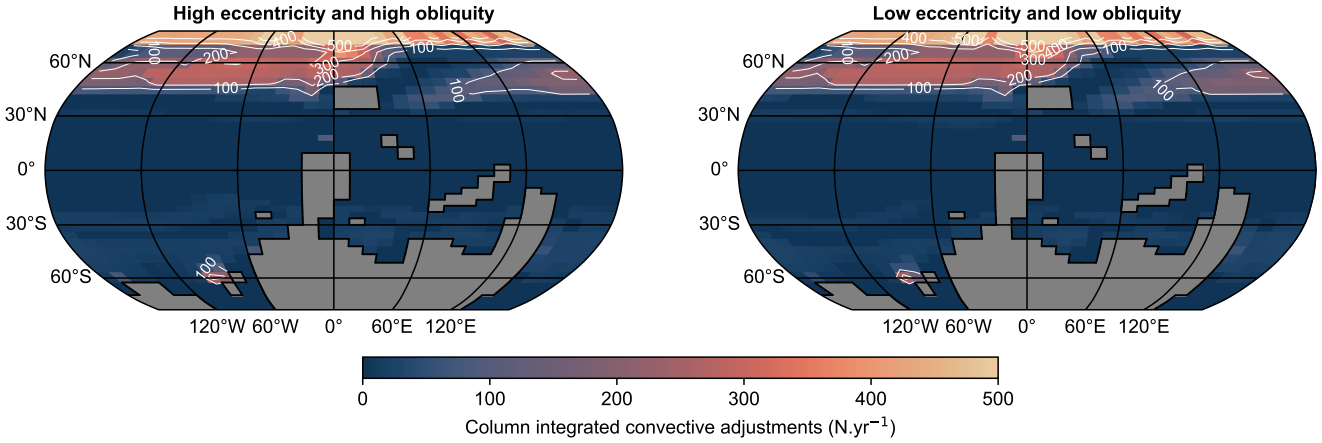


**Figure A2. Deep water formation.** Convective adjustments (expressed as the number of convective adjustments integrated across the water column per year) for **(a)** high eccentricity-high obliquity and **(b)** low eccentricity-low obliquity astronomical configurations.

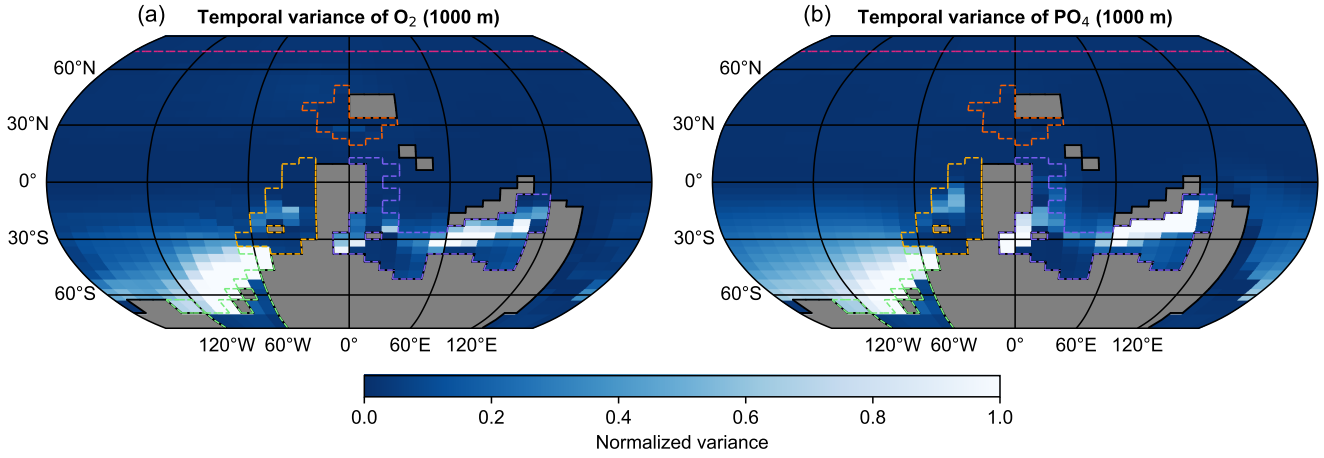


**Figure B1. Temporal variance.** Normalized temporal variance of **(a)** [$O_2$] and **(b)** [$PO_4$] averaged over the upper 1000 m. Dashed coloured lines indicate regional boundaries, as defined in Fig. 4.